Saharan dust in night-time thermal imagery: detection and correction of related biases in retrieved sea surface temperature

C J Merchant and O Embury
Institute for Atmospheric and Environmental Science, The University of Edinburgh

P Le Borgne and B Bellec
Centre de Meteorologie Spatiale, Meteo-France

1 Introduction

Practitioners of operational meteorology, oceanographers and climatologists make extensive use of sea surface temperatures (SSTs) estimated from thermal images collected by space-borne sensors. Users' requirements for the accuracy of SST analyses steadily become more demanding, and, as a result, the differing bias characteristics of various SST products are subject to greater scrutiny in the context of initiatives such as the Global Ocean Data Assimilation Experiment High Resolution SST Pilot Project (GHRSST-PP, see www.ghrsst-pp.org). In the case of thermal infrared sensors, biases can include those originating from error in specifying retrieval coefficients [Merchant and Le Borgne, 2004], prior error and non-linearity error [Eyre, 1987; Merchant et al, 2005b], undetected cloud [e.g., Simpson et al, 1998; Merchant et al, 2005a], stratospheric aerosol [e.g., Walton et al, 1998; Merchant et al, 1999; Merchant and Harris, 1999], near-surface stratification (if the target is estimation of the bulk SST) [e.g., Murray et al, 2000; Gentemann et al, 2003] and – the subject of this article – tropospheric aerosols [e.g., Nalli and Stowe, 2002; Vazquez-Cuervo et al, 2004]. Saharan dust is a mineral tropospheric aerosol intermittently lofted from the Saharan desert in air streams that transport the dust over the equatorial and north Atlantic ocean. The dust can be carried in significant concentrations as far as, for example, the Caribbean or Scotland. Among the effects of the presence of Saharan dust in the atmosphere is a modification of up-welling radiation over a broad range of thermal wavelengths that includes the "windows" used for remote sensing of SST [e.g., Deschamps and Phulpin, 1980].

The Spinning Enhanced Visible and Infrared Radiometer (SEVIRI) is the imaging sensor that operates on the meteorological satellite, Meteosat 8. From SEVIRI imagery, the Ocean and Sea Ice Satellite Application Facility (OSI-SAF) generates a range of products at ~10 km spatial resolution over a full Earth disk, on a 3 hourly cycle. SST is among these products, and since the Meteosat-8 platform is in geostationary orbit at 0° longitude, all Saharan dust outbreaks occur within the SEVIRI field of view. As we will show in this article, Saharan dust has caused biases ~1 K in OSI-SAF SSTs during the initial phase of Meteosat-8 operations.

While the presence of dust can be readily detected in day-time imagery by the increase in clear-sky albedo over the ocean using visible channels [e.g., Tanre et al, 1997; Waquet et al, 2005], the detection of dust contamination in night-time imagery must rely only on its impact on thermal wavelengths. This article explains the new method we have developed to identify significant dust over the ocean in SEVIRI night-time imagery and describes how the corresponding impacts on SST retrieval can be reduced. We begin (in section 2) by describing an investigation of the likely effects of dust contamination on SEVIRI radiances, using radiative transfer modelling. This allows us to define a brightness-temperature space in which the impacts of dust are more apparent and in which we then compare simulations and observations for dust-free and dusty atmospheres (in section 3). On this basis, we define a dust-contamination metric which we shown to be strongly related to biases in SEVIRI SSTs and which correlates spatially with other available aerosol indices (section 4). Finally (in section 5), we propose a strategy for improved retrievals of SST in the dust-affected region, via a mix of screening more-contaminated areas and use of coefficients that are less sensitive to aerosol effects on up-welling radiance.

2 Simulation of dust-affected brightness temperatures

2.1 Approach

For SST retrieval, it is customary to express channel-integrated top-of-atmosphere radiance as brightness temperature (BT), i.e., as the temperature a perfect black-body would need to be to emit the observed channel-integrated radiance. This significantly linearizes the retrieval of SST [e.g., Zavody et al, 1995]. Cloud detection schemes also tend to be expressed in BT [e.g., Saunders and Kriebel, 1988; Zavody et al, 2000]. In this paper, therefore, we express the radiative effects of Saharan dust in terms of the change in brightness temperature caused by the presence of the dust compared to dust-free clear skies.

We begin exploring the effects of Saharan dust on BT using radiative transfer simulations. Our objective is to characterize the relative magnitudes of change in BT in the relevant SEVIRI thermal channels caused by the presence of dust. In simulation, we can explore systematically the effects of factors such as aerosol optical depth (AOD), aerosol absorption and scattering characteristics, and the aerosols' height distribution. Generally, we can expect such factors to influence different channels differently. As a result, biases in SST and other products estimated from these BTs will be variable, and not simply related to AOD, for example.

Our focus here is on improving SST retrievals from SEVIRI. SST retrievals are generally formed using an estimator that is a weighted combination of the BTs in different channels and/or differences in BT between various channel pairs [e.g., Barton, 1995]. These can all be expressed as follows [Merchant et al, 1999]:

$$\hat{x} = a_0 + \mathbf{a}^{\mathbf{T}}\mathbf{y} \qquad (1)$$

where $\hat{x}$ is the estimated SST, a_0 is an offset coefficient, $\mathbf{y}$ is a vector listing the BTs of all the channels used, and $\mathbf{a}$ is a vector of coefficients (weights). For thermal sensors, the channels used typically include 3.7, 11 and 12 µm; for SEVIRI, there is a 3.9 µm channel that is significantly broader than corresponding channels on other sensors, and also an 8.7 µm channel that may be used for SST. Here, then, $\mathbf{y}^{\mathbf{T}} = [y_{3.9} \quad y_{8.7} \quad y_{11} \quad y_{12}]$. Depending on the formulation, the coefficients may be functions of the satellite zenith angle, the prior ("guess") SST, etc. Assume that the coefficients are well specified, and therefore give near-zero bias when applied to the BTs observed under conditions of clear sky and negligible aerosol. Let the effect on BTs of a particular instance of Saharan dust in the atmospheric column be $\mathbf{k}$ so that the BTs are modified to $\mathbf{y}_{aer} = \mathbf{y} + \mathbf{k}$, where the subscript *aer* indicates BTs in the presence of significant aerosol. (Since the effect of aerosol is usually to lower the BT, the elements of $\mathbf{k}$ will usually be negative.) The corresponding bias in SST is then [Merchant et al, 1999]:

$$\Delta\hat{x} = \mathbf{a}^{\mathbf{T}}\mathbf{k} \qquad (2)$$

Depending on the signs and magnitudes of the retrieval coefficients and thus on how the aerosol impacts on different channels are weighted and combined, the bias corresponding to the presence of aerosol can therefore be positive, zero or negative. In practice, the usual outcome is negative bias, with near-zero bias only arising by design [Merchant et al, 1999].

The simulations amount to an evaluation of $\mathbf{k}$. This is achieved by running a radiative transfer model (our "forward model") for a sample of "clear-sky" atmospheric profiles with aerosol present, and then subtracting from the resulting BTs the BTs of the corresponding aerosol-free simulations.

2.2 Forward Model

A forward model for simulating clear-sky aerosol-modified BTs must represent thermal emission (by the surface, atmospheric gases and aerosols), reflection (of down-welling radiance at the surface), absorption (by gases and aerosol) and scattering of radiation (by aerosols). At the Centre de Meteorologie Spatial (CMS), the fast forward model RTTOV [Saunders et al, 1999] is used for many purposes including to define SST retrieval coefficients, so it is advantageous to use it for this study. However, the standard current version of RTTOV does not represent scattering processes in the infrared, and so the first task was to extend the capability of the model. We did this by modifying the scattering code already implemented within RTTOV for scattering of microwave radiation within clouds (a delta-Eddington approximation [Bauer, 2002]) to work for infra-red wavelengths. (The microwave implementation assumed the Rayleigh-Jeans approximation, which is not valid for the thermal infra-red spectrum.) The delta-Eddington approximation for scattering assumes a phase function (i.e., angular distribution of scattering angle) that is a simple, smooth function of the asymmetry parameter, g. ($\frac{g+1}{2}$ is the fraction of scattered radiation that is scattered into the forward hemisphere.) Two further aerosol properties need to be defined: the single scattering albedo, ω, (which describes the probability of a scattering interaction) and the extinction coefficient, β, (the attenuation of radiance per unit length). {*More details are given in Appendix 1.*}

For Saharan dust, we define the values of g, ω and β using tabulated values for transported mineral aerosol from OPAC [Hess et al, 1998] and, for comparison, values derived using Mie theory [Mie, 1908] applied to observations from the AERONET [Highwood et al, 2003] site at Dahkla. (The Mie calculations come courtesy of J Haywood and A O'Carroll at the Met Office, and hereafter these parameters are referred to as the "Haywood" parameters.) The curves of these parameters are shown in Figure 1. A single value of each of g, ω and β is required by RTTOV for each channel, and the values weighted by the sensor spectral response functions are used. Given the general nature of the OPAC tabulation and the localized nature of the Dahkla observations, the overall features are fairly consistent, although there are significant differences in absorption coefficient in the 10.5 to 12.5 μm window that will affect the relative impacts on the "split window" channels.

The final part of the forward model is the specification of the surface and atmospheric state. We perform the simulations on a set of 365 global ocean profiles; these are the "SAFREE" profile set [Brisson et al, 2002] used to define SST retrieval algorithms for the OSI-SAF (with profiles from latitudes poleward of 60° excluded). For each profile in the set, a simulation is performed with three air-sea temperature differences: -3, 0 and +3 K. The vertical profiles of dust that we use are simply idealized examples, in which aerosol is present over a layer 1 km deep, with the lower altitude of the layer at 0, 1, 2, or 3 km above the surface. The total AOD contributed by this 1 km layer is varied from 0.0 (aerosol free calculation) to 1.0. (The AOD used in this article is that at 10 μm, and corresponds to $\tau_{10} = 0.52\tau_{0.55}$ [Haywood et al, 2005]). Simulations are performed at several satellite zenith angles between 0° and 72°.

2.3 Results

Table 1 shows the mean simulated change in BT from the presence of a Saharan dust layer with AOD of 0.3 at 10 μm, for base heights of the aerosol layer from 0 to 3 km of altitude, using aerosol characteristics from both OPAC and Haywood. Over this range of base heights, the change in BT is roughly linear with respect to height. The main effect of changing height is to alter the BT of emitted radiance from the aerosol.

The differences between the channels can be interpreted with reference to the single scattering properties (SSPs) shown in Figure 1. Firstly, the 3.9 µm channel shows almost no variation with base height. This is because ω is very high (>0.9 for both Haywood and OPAC characteristics) so the aerosol effect is almost entirely due to scattering. Secondly, the 8.7 µm channel, which (in contrast to the 3.9 µm channel) has the lowest single scattering albedo, shows the greatest change in BT with base height. Thirdly, the variation with height in the 11 µm channel is similar despite the SSPs being markedly different. This is because the impact is dominated in this thermal window region by absorption, and the absorption coefficient, ($\beta_{abs} = (1-\omega)\beta$), is about equal for OPAC and Haywood. In contrast, the absorption coefficient is differs between OPAC and Haywood at 12 µm, and thus the rate of change in BT with height is markedly different between the simulations for this channel.

The degree of linearity of the change in BT with respect to AOD is illustrated in Figure 2, where the mean BT change is plotted against AOD for the four SEVIRI window channels. For all AODs considered the change is nearly linear. Over this range, therefore, for a given atmospheric state and vertical aerosol distribution, we can write

$$\mathbf{k} = \delta c \hat{\mathbf{k}} \tag{3}$$

where δ is the AOD, $\hat{\mathbf{k}}$ is $\mathbf{k}$ normalised, and c is a scaling constant between AOD and the change in BTs. In Merchant et al [1999], the insight that the impacts of stratospheric aerosol on window BTs could be expressed in this way allowed the authors to define SST retrievals that were "robust" (i.e., insensitive to the aerosol). This worked because, for stratospheric aerosol, $\hat{\mathbf{k}}$ is fairly invariant (for a given age of the aerosol). However, the situation with respect to lower tropospheric aerosols is less favourable, because there is a greater effect on $\hat{\mathbf{k}}$ associated with the atmospheric profile of water vapour and temperature, and with the vertical distribution of aerosol, factors that are less influential in the case of stratospheric aerosol. In addition, of course, in the troposphere there is also a greater variability in the aerosol properties (i.e., there is a greater variety of particle size distributions and infra-red refractive indices).

In order to distinguish BTs that have been modified by the presence of dust from those unaffected, it is useful to find a transformation of $\mathbf{y}$, let's call it $\tilde{\mathbf{y}}$, in which variability introduced by dust is more obviously different from variability associated with the atmospheric profile of water vapour and temperature. In Figure 3, we plot the location of simulated BTs on a graph of BT differences (BTDs), with the 3.9 µm BT minus the 8.7 µm BT on the ordinate and the 11 µm BT minus the 12 µm BT on the abscissa. All the clear-sky aerosol-free simulations are plotted here (with added Gaussian noise corresponding to the noise equivalent differential temperatures of each SEVIRI channel), and form a fairly tight and linear locus of points. For six example profiles, the simulated effect of introducing aerosol with a base height of 2 km is shown, using both OPAC and Haywood aerosol properties, for a range of AODs. In general, aerosol has the effect of decreasing the 11-12 µm BTD and increasing the 3.9-8.7 µm BTD. In rare cases, such as the profile in the bottom left of the figure, the effect can be reversed. This only occurs for a small fraction (about 2%) of profiles in this area – although the frequency increases for lower aerosol base height and higher SZA. Dust-affected simulations for AODs greater than about 0.3 are seen clearly to stand out from the locus of aerosol-free simulations in this space for simulations based on the Haywood parameters. They stand about because the aerosols' effects on BTs as expressed in this space, $\tilde{\mathbf{k}}$, is in a different direction to the principal axis of the distribution of aerosol-free simulations. A generalisation of the concept illustrated by Figure 3 forms the basis of the technique for identifying dust-affected observations explained in the following section.

3 An index for Saharan dust

3.1 Definition of the index

In Figure 3, the simulations for the OPAC aerosol parameters are less separated from the locus of aerosol-free BTDs than those using the Haywood aerosol parameters. However, one could identify a different BTD space in which the converse is true (not shown). Moreover, as we find below, observed impacts on BTDs of Saharan dust are somewhat different again. In order to define an index for the presence of dust, we generalize the concept of Figure 3 to three dimensions, there being a maximum of three independent BTDs that one can form from four BTs. This increases the likelihood that the aerosol impact is able to be discriminated.

There are sixteen unique definitions of a three-dimensional BTD space that can be defined from four BTs (not counting different orderings as different spaces). It will be convenient to choose a space that includes the difference between the 11 and 12 μm BTs (since this difference appears in the operational SST estimator) and in which the locus of aerosol-free BTDs is as linear as possible. Other things being equal, the more linear the locus of aerosol-free BTDs, the greater the percentage of variance explained by the first principal component of the aerosol-free BTD variability. We therefore calculated the percentage of variance explained for each possible BTD space, and select our three-dimensional BTD space on this basis to be:

$$\tilde{\mathbf{y}} = \begin{bmatrix} y_{3.9} - y_{8.7} \\ y_{3.9} - y_{12} \\ y_{11} - y_{12} \end{bmatrix} = \begin{bmatrix} 1 & -1 & 0 & 0 \\ 1 & 0 & 0 & -1 \\ 0 & 0 & 1 & -1 \end{bmatrix} \mathbf{y} \equiv \mathbf{T}\mathbf{y} \tag{4}$$

where **T** is a transformation matrix which is implicitly defined by this expression. Similarly, the effect of the presence of aerosol in this space is $\tilde{\mathbf{k}} = \mathbf{T}\mathbf{k}$.

The locations of the simulated BTDs (including simulated instrumental noise), $\tilde{\mathbf{y}}$, are shown in Figure 4, along with the principal axis of variability in the data (i.e., the first principal component (PC)). 99% of the variance in this BTD space is associated with the location of points along this axis. The remaining 1% of variance is associated with the off-axis variability, and the RMS perpendicular distance from the points to the line is 0.30 K.

The basis of our Saharan dust index (SDI), then, is to be the distance of an observed point from the domain spanned by aerosol-free observations. Since PCs are orthogonal to each other, the distance is conveniently found using the projections of the BTDs onto the second and third PCs, as follows.

Let $\mathbf{S}_{\tilde{\mathbf{y}}\tilde{\mathbf{y}}}$ be the covariance matrix of $\tilde{\mathbf{y}}$. (We use here the convention adopted in Merchant et al [1999] that covariance matrices are represented by a bold "S", with the covariant variables given in the subscript.) The eigenvectors of $\mathbf{S}_{\tilde{\mathbf{y}}\tilde{\mathbf{y}}}$ are then the principal components of the BT differences. Each PC is a 3-element vector in the BTD space; define **P** as the 3-by-3 matrix whose rows are the PCs. (We adopt the convention here that the PCs are normalized to unit length, and their weights have dimension.) **P** can then be used to achieve a transformation of the BTD co-ordinates:

$$\mathbf{y}' = \mathbf{P}\left(\tilde{\mathbf{y}} - \bar{\tilde{\mathbf{y}}}\right) = \begin{bmatrix} 0.758 & -0.577 & 0.303 \\ 0.425 & 0.085 & -0.901 \\ -0.495 & -0.812 & -0.310 \end{bmatrix} \left(\tilde{\mathbf{y}} - \bar{\tilde{\mathbf{y}}}\right) = \mathbf{P}\mathbf{T}\left(\mathbf{y} - \bar{\mathbf{y}}\right) \tag{5}$$

where: an over-bar indicates an average (across the set used to define $\mathbf{S}_{\tilde{\mathbf{y}}\tilde{\mathbf{y}}}$); and the elements of $\mathbf{y}'$ are the weights of the respective PCs for the "observed" BTDs. The numerical values of the PC vectors are given in the rows of the explicit matrix in this expression, with the most significant PC in the top row, the least significant in the bottom row. Again, modulations of BT by the presence of dust are transformed in the same way: $\mathbf{k}' = \mathbf{PTk}$. By construction, y_1' (the weight of the first PC) is highly variable for aerosol-free BTDs (square root of variance is 2.36 K), since it captures the main variability of the BTDs associated with the clear-sky atmospheric profiles of water vapour and temperature. Tropospheric aerosol could well cause observations to shift along this axis, but such impacts are unobservable on the basis of the BTs alone: if **PTk** is or is approximately equal to $[1 \quad 0 \quad 0]^T$, then the aerosol is undetectable (at least without other detailed prior information). On the other hand, the aerosol-free variability in y_2' and y_3' is modest (square roots of variances are $\sigma_2 = 0.26$ and $\sigma_3 = 0.19$ K, respectively). Tropospheric aerosols that cause observations to shift along these axes are observable. On the basis of the results shown in Figure 3, there is reason to expect that Saharan dust will often be observable in this sense (which is confirmed below).

Figure 5(a) is a scatter plot of y_3' versus y_2' for the aerosol-free simulations. An ellipse corresponding to a 2σ threshold has been plotted, and most of the aerosol-free simulations fall within it. The SDI will be related to the location within this space.

Figure 5 (b) illustrates how simulated dust-affected BTDs are located on this plane, for a few combinations of AOD, base height of the dust layer and aerosol parameters based on OPAC and Haywood. There are cases where dust-affected BTDs nonetheless lie within the "aerosol-free" ellipse and cannot be detected. However, most of the dust-affected BTDs are well outside the ellipse and are detectable.

It appears that increasing the AOD affects the distance of the point in the y_3' versus y_2' plane to the centre, and the aerosol height affects the direction. As the aerosol type (OPAC v. Haywood) can also affect the angle of displacement, it seems that the SDI should be based on the distance from (0,0), with the angle possibly supplying some additional information. However; before we can verify this using observed BTs, it turns out to be necessary to correct the y_2' and y_3' values for simulation bias and zenith angle, as explained in the next sections.

3.2 Empirical adjustment

In the previous sections, we have explored the distributions of simulated BTDs, and devised a method for deriving an index that measures deviations from the clear-sky aerosol-free distribution. However, forward model errors are typically of order 0.1 K for thermal window channels [Merchant and Le Borgne, 2004], and may be greater if, for example, the characterisation of the sensor response is flawed. Therefore, we must now confront the index based on simulations with real observations, and make any adjustments necessary.

Sequences of SEVIRI imagery can be interpreted by experts such that Saharan dust, other aerosols and various cloud types can be identified and tracked. Conversely, portions of imagery that are highly likely to be clear-sky can also be identified. Here we use the Interactive Test data supplied by H. LeGléau of Meteo-France. Also, because it can be a very subjective judgement to identify aerosol events "by eye" in night time imagery, the OSI-SAF SST match-up database (MDB) [Brisson et al, 2002] was used as a second source of putative clear-sky data. To select aerosol-free data, only points where the SEVIRI retrieved SST was within 2 K of the SST measured by a corresponding buoy are used.

Figure 5 (c) and (d) show the location of these aerosol-free SEVIRI images in the plane of y_3' versus y_2'. There is a discrepancy that causes the observations to lie outside of the ellipse expected for aerosol-free BTs. It is necessary to correct the simulations for whatever bias causes this to be the case. We find that reducing the simulated BTs for the 8.7 µm channel by 0.6 K brings the observations into good agreement with the simulations, both in the plane of y_3' versus y_2' (see Figure 5 (e) and (f)), and in other checks for consistency of the simulations and observations (not shown here). Whether there is really a bias of -0.6 K in the RTTOV simulations of this channel is a question that remains open at present: it could equally be that this adjustment is somehow compensating for biases in other channels, or that there is a calibration issue in that channel. However, it is a simple adjustment, in that $\bar{\mathbf{y}}$ is changed in equation 6 but not **P**, and it is convenient and effective to proceed on this basis.

3.3 Higher zenith angles

All of the above results pertain to simulations at a satellite zenith angle (SZA) of 0°, and observations within 30° of nadir. SST retrievals are obtained from SEVIRI at SZAs up to 72°. As mentioned before, Saharan dust is often transported across the Atlantic ocean to the Caribbean seas, and the SZA for the Caribbean seas is ~60° from the Meteosat-8 orbit. The index must therefore be adapted to SZAs that are not nearly vertical.

In simulation, it was found that the direction of the first PC in BTD space was almost invariant with respect to changing SZA up to 60°. For simplicity, therefore, the PCs defined implicitly in equation (5) are used for SZAs from 0° to 60°; this avoids having to parameterize the variation in the PCs with respect to SZA. When aerosol-free simulations of BTDs at higher angles are projected onto the PCs, it is found that the locus of points in the plane of y_3' versus y_2' drifts away from being centred on (0, 0), as a result of the first PC being no longer exactly equal to the main axis of variability of the higher-angle observations. The corresponding ellipses are shown in Figure 5(g), for 0°, 36.9°, 48.2°, 55.2° and 60°. These angles correspond to *S* equal to 0, 0.25, 0.5, 0.75 and 1.0, where $S = \sec(\theta_{SZA}) - 1$. The higher-angle ellipses drift linearly with respect to *S*. The widths of the ellipses also increase with increasing SZA, and again this is adequately parameterized as linear with respect to *S*. This extension to higher zenith angles looks satisfactory in comparison with aerosol-free SEVIRI observations with higher SZAs (see Figure 5(h) and (i)).

In order to adapt the index for higher zenith angles two corrections are used. Firstly, we correct the offset such that the clear-sky ellipses are always centred on (0,0). Secondly, the second and third PCs are scaled such that the variance along each is constant with SZA.

It was found that this method of correction gave good results for SZA below 60°. Between 60° and 72° the method should be used with caution as clear-sky points begin to be found outside the ellipse more frequently. For SZA over 72° our method cannot be considered valid.

3.4 Preliminary verification of index

We now need to define a Saharan Dust Index (SDI) based on the location of observed points in the PC plane after adjustment as outlined in sections 3.2 and 3.3. Figure 6 (a) shows data from several regions plotted in the PC plane (note only pixels classified as clear by the SEVIRI cloud mask are shown), Figure 6 (b) shows where these regions are located in the SEVIRI FOV.

Regions A, B, C, and E all correspond to confirmed aerosol events. Region D is not a confirmed aerosol event, but it is located in an area where aerosol events occur. Figure 6 (c) shows a scatter plot of pixels from other confirmed aerosol events. In all cases aerosol seems to be characterised by $y_2' > 2\sigma_2$. For these cases, y_3' is generally positive for aerosol. Region F is in an area which could be affected by sand aerosol but is not thought to be in this case (more details given below). Region G is mostly cloudy; even though only ‘clear-sky’ pixels are shown in Figure 6 (a), the region is almost entirely outside the 2σ ellipse. This behaviour is often seen in pixels near the edge of the SEVIRI cloud mask. It is thought to be caused by thin, unscreened cloud, or areas of high humidity near to clouds. Region H actually corresponds to two separate locations in the SEVIRI FOV, this was done because they were indistinguishable in the PC plane, and both regions are partially cloudy. These regions includes both pixels inside the clear-sky ellipse (it almost completely overlaps Region I) and significantly outside the ellipse. Although they come from an area often affected by smoke aerosol, the pixels outside the 2σ ellipse are seen in imagery (not shown) to be fringing clouds and do not appear to be related to smoke aerosols.

Region I corresponds to four areas of largely cloud-free sky believed to be free of any aerosol. In the PC plane, the Region is within the 2σ ellipse. There is a displacement of order 0.2 K towards negative values of y_2' and y_3'; this may reflect residual biases between clear-sky simulations and observations that have not been completely corrected by the empirical adjustment of section 3.2.

The evaluation of the PC data as a means of monitoring Saharan Dust events is ongoing operationally at CMS. This involves comparison of the data with other AOD products and experimental use by meteorologists for tracking events. The objectives include gaining a more complete understanding of: how y_2' and y_3' relate to AOD estimates based on quite different radiative signatures; of when and where y_2' and y_3' give false detection and/or fail to detect dust; and of how y_2' and y_3' respond to other aerosols such as from biomass burning. These are all important questions and, depending on their answers, the y_2' and y_3' values may have applications beyond the issue of addressing dust-related biases in SST. However, they are beyond the scope of this article, which is focussed on the application of an SDI to reducing dust-related biases in SEVIRI SSTs. Thus, in this present work, we define our SDI to be, simply, equal to y_2', because the displacement caused by Saharan dust is mainly along this second PC. (The fact that the displacement is nearly aligned with the second PC is a coincidence; recall that the PC analysis was performed using only clear-sky aerosol-free simulations.) Note also from Figure 6(a) that the Saharan dust events are all associated with positive values of this index.

4 Comparison of index with MODIS AOD

Before considering SST biases in the light of the SDI, it is instructive to perform some comparison of the SDI with AOD retrievals from the MODIS Aqua AOD product. This product was chosen as is has been extensively compared with AERONET observations and found to be highly accurate [Ichoku et al, 2005].

The MODIS AOD daily product is available on a 1° by 1° grid. In order to compare the SDI with this, a SDI nightly product was produced on the same grid. Figure 7 shows the two products for 10 days at the end of July 2005. Visually there is good agreement between the two, with the exception of biomass burning aerosol present in the Gulf of Guinea visible in the MODIS imagery. The progress of Saharan dust events across the Atlantic and Mediterranean can be observed in both products. Variation of the aerosol over the Red Sea and Indian Ocean is difficult to see, but aerosol is clearly detected by both satellites.

There are some areas with high SDI which does not appear to be aerosol. High SDIs appear in the North Atlantic for zenith angles >70º, but as already noted, we don’t claim the method is applicable at these angles. High SDIs can also be seen in the South Atlantic just off the coast of Namibia. This region is adjacent to a desert and so could be contaminated by sand aerosol. However, the feature does not vary significantly with time and elevated AODs are not present in the corresponding visible imagery. Figure 6 (d) is a scatter plot of the second and third principal components for data extracted from this region, and shows that y_3' is lower than found in confirmed aerosol regions (see Figure 6 (c)). The high SDI is probably caused by relatively unusual surface and atmospheric conditions: a cold upwelling reduces the SST in the region and the atmosphere is relatively dry.

Figure 8 shows plots of the SDI against the MODIS measured AOD. In order to compare the night time data with the daytime data each 1° by 1° cell in the night time SDI compared against the average of the corresponding daytime MODIS AOD cells (for the day before and day after). If a cell was not observed for both days (either due to cloud, or the daily coverage of MODIS) then it is rejected. Results have been binned in intervals of 0.1 MODIS AOD and are shown for various ranges of zenith angle.

For MSG zenith angle less than 24°, which mainly covers the biomass burning aerosol in the Gulf of Guinea (see Figure 9), there is little correlation between the SDI and the AOD. However; for all other ranges of zenith angle there is a clear linear relationship, up to a MODIS AOD of 0.6 or 0.7, above which the SDI remains roughly constant. This upper limit may correspond to the point at which aerosol is detected by the SEVIRI cloud mask: pixels with higher values of SDI are flagged as cloud and are not included in the comparison. It so happens that the slope of the SDI-AOD relationship over the linear range is such that SDI and MODIS AOD have comparable numerical values.

Figure 8 (b), (c), (d) (which correspond to zenith angle ranges of 24°-48°, 48°-60°, and 60°-72° respectively) show that SDI-AOD relationship changes slightly, both in its slope and in its intercept (i.e., the average SDI for a MODIS AOD of 0.0). The size of the change in the intercept is ±0.1, the same magnitude as the errors in fitting the offset of the clear-sky ellipse with respect to satellite zenith angle (see section 3.3). A more constant SDI-AOD relationship could perhaps be obtained by 'scaling' the SDI, but the SDI would still remain sensitive to factors other than the AOD. Figure 10 shows plots of SDI against visible AOD for simulations using the Haywood optical properties. Varying the zenith angle has a relatively small effect on the SDI-AOD relationship, while the height of the aerosol layer has a much stronger effect. Similarly, changes in the nature of the aerosol will also affect the SDI-AOD relation. As the different zenith angle ranges correspond to different geographically locations, we should also expect them to correspond to different vertical distributions and compositions of aerosol.

5 Use of index to improve SST retrievals

5.1 Existing SST bias and Saharan dust index

In the OSI-SAF match-up data base for SEVIRI SSTs, there is a clear connection between the new SDI and SST biases, as shown in Figure 11. For a given range of SZA, there is in increasing tendency to negative SST bias as the SDI increases. The standard deviation also increases for positive SDI, while for negative SDI it is nearly constant, reflecting the fact that there is not a one-to-one relationship between SDI and bias.

For a SDI of zero the SST bias is also very close to zero expect at zenith angles less than 24°. (There are far fewer match-ups in the range of zenith angle less than 24°, and this area is more strongly affected by smoke aerosol. It may be the case that smoke aerosol could affect the SST bias, while having little effect on the SDI.) For values of SDI below -0.3, the SST bias appears to be roughly constant at ~0.2K. These values of SDI lie outside the range expected from clear-sky simulations and (as noted above) tend to fringe areas of detected cloud.

For values of SDI above 0.3 the SST bias rapidly increases with SDI. This is seen most clearly for SZA between 24° and 48° – the range most affected by Saharan dust (refer to Figure 9). The bias-SDI relationship appears to break down when the SDI is greater than ~0.8 – i.e., as the cloud detection algorithms start flagging aerosol as cloud. For SDIs between about 0.3 and 0.8, the relationship between bias and SDI is close to linear.

Note that the details of the bias-SDI relationship depend on the SST retrieval coefficients used: the sensitivity of different coefficients to the dust varies. We can analyze the effect on SST of aerosol impacts using equation 2. Operational retrievals of SST for the OSI-SAF are made using an algorithm whose coefficients depend on a climatological SST for the place and time observed and on SZA. For the main Saharan dust region over the Atlantic west of Saharan Africa in July, we have $\mathbf{a} = [0 \quad 0 \quad 3.07 \quad -2.08]^{T}$, i.e., the retrieval is a “split window” algorithm that depends only on the 11 and 12 μm channels. We can derive estimates of the range of bias expected from our simulations using the **k** vectors such as those in **Error! Reference source not found.**, but for the appropriate SZA (around 36°). The results along with their values of SDI are listed in Table 2 for an AOD at 10 μm of 0.25 (roughly corresponding to a visible AOD of 0.5).

The predicted SST biases are similar to biases in AVHRR retrievals of SST found by Highwood et al [2003]. The authors examined the effect of Saharan dust by looking at SST retrievals during five days as an aerosol event passed over an area of the Atlantic Ocean and found the SST bias due to aerosol was greater than 3 K. As the AVHRR retrieval is also a split window” algorithm we expect it to be affected by aerosol in a similar way.

The large SST biases predicted by simulations are not seen the in MDB. We believe this is because OSI-SAF uses a modified version of the SEVIRI cloud mask which is much more sensitive to clouds than the standard cloud mask (the results in Section 4 used the standard SEVIRI cloud mask). One of the additional checks in the modified cloud mask is a comparison against a SST climatology, this will remove the aerosol cases with large SST biases.

6 Conclusion and Further Work

Aerosols such as Saharan dust can have a significant effect on satellite SST retrievals. Although cloud screening algorithms will often detect thick layers of aerosol, biases of 1-3 K will remain depending on the algorithm used.

We have proposed a method to identify Saharan dust in night-time imagery from the SEVIRI instrument using only thermal IR channels. There is a strong spatial correlation between the SDI calculated using SEVIRI data and AOD measured by the MODIS instrument except in areas known to be affected mainly by smoke aerosol rather than dust aerosol. The SDI can also be related to satellite SST retrieval biases. The SST bias caused by aerosol appears to be smaller in the OSI-SAF SST match-up database due to the more rigorous cloud screening algorithm. However; not all aerosol is detected by this cloud mask, and the remaining biases are strongly correlated to SDI.

The impact of aerosol on SEVIRI SST retrievals has not been fully investigated yet. Further work should include quantifying the SST impact (a method similar to Highwood et al. [2003] would seem sensible). The discrepancy between the MDB bias and predicted bias needs to be resolved, which should be possible by applying a different cloud screening algorithm.

Acknowledgements

We gratefully acknowledge that J. Haywood and A. O’Carroll of the Met Office supplied optical properties of Saharan Dust based on observations of the AERONET site at Dahkla.

References

Barton, I.J., 1995, Satellite-Derived Sea-Surface Temperatures - Current Status, *Journal of Geophysical Research-Oceans*, 100, p. 8777-8790.

Bauer, P., 2002, Microwave radiative transfer modeling in clouds and precipitation, Part I: Model description. Satellite *Application Facility for Numerical Weather Prediction*, NWPSAF-EC-TR-005.

Brisson A., Le Borgne P., and Marsouin A., 2002, Results of one year of preoperational production of sea surface temperatures from GOES-8, *J Atmos Ocean Tech*, 19 (10): 1638-1652.

Deschamps, P.Y. and Phulpin, T., 1980, Atmospheric correction of infrared measurements of sea surface temperature using channels at 3.7, 11 and 12 µm, *Boundary-Layer Meteorology*, 18, p. 131-143.

Eyre, J.R., 1987, On systematic errors in satellite sounding products and their climatological mean values, *Q. J. R. Meteorol. Soc.*, 113, 279–292.

Gentemann, C.L., Donlon, C.J., Stuart-Menteth, A., and Wentz, F.J., 2003, Diurnal Signals in Satellite Sea Surface Temperature Measurements, *Geophysical Research Letters*, 30, p. art. no.-1140.

Haywood, J.M., Allan, R.P., Culverwell, I., Slingo, T., Milton, S., Edwards, J., and Clerbaux N., 2005, Can desert dust explain the outgoing longwave radiation anomaly over the Sahara during July 2003?, *J. Geophys. Res.*, 110, D05105, doi:10.1029/2004JD005232.

Hess, M., Koepke, P., and Schult, I., 1998, Optical Properties of Aerosols and clouds: The software package OPAC, *Bull. Am. Met. Soc.*, 79, 831-844.

Highwood, E.J., Haywood, J.M., Silverstone, M.D., Newman, S.M., and Taylor, J.P., 2003, Radiative properties and direct effect of Saharan dust measured by the C-130 aircraft during Saharan Dust Experiment (SHADE): 2. Terrestrial spectrum, *J. Geophys. Res.*, 108(D18), 8578, doi:10.1029/2002JD002552.

Ichoku, C., Remer, L.A., Eck, T.F., 2005, Quantitative evaluation and intercomparison of morning and afternoon Moderate Resolution Imaging Spectroradiometer (MODIS) aerosol measurements from Terra and Aqua, *J. Geophys. Res.*, 110 (D10S03), Correction published 26 March 2005

Merchant, C.J., Harris, A.R., Murray, M.J., and Zavody, A.M., 1999, Toward the Elimination of Bias in Satellite Retrievals of Sea Surface Temperature 1. Theory, Modeling and Interalgorithm Comparison, *Journal of Geophysical Research-Oceans*, 104, p. 23565-23578.

Merchant, C.J., and Harris, A.R., 1999, Toward the Elimination of Bias in Satellite Retrievals of Sea Surface Temperature 2. Comparison With in Situ Measurements, *Journal of Geophysical Research-Oceans*, 104, p. 23579-23590.

Merchant C.J., Harris A.R., Maturi E., and MacCallum, S., Probabilistic physically-based cloud screening of satellite infra-red imagery for operational sea surface temperature retrieval, *Quart. J. Royal Met. Soc.*, accepted June 2005a.

Merchant C.J., Horrocks, L.A., Eyre, J., and O'Carroll, A.G., 2005, Retrievals of sea surface temperature from infra-red imagery: origin and form of systematic errors, *Quart. J. Royal Met. Soc.*, submitted 2005b.

Merchant, C.J., and Le Borgne, P., 2004, Retrieval of Sea Surface Temperature From Space, Based on Modeling of Infrared Radiative Transfer: Capabilities and Limitations, *Journal of Atmospheric and Oceanic Technology*, 21, p. 1734-1746.

Mie, G., 1908, Beitrage zur Optic truber Medien, speziell kolloidaler Metallosungen, *Ann. Phys.*, 30, 377-442.

Murray, M.J., Allen, M.R., Merchant, C.J., Harris, A.R., and Donlon, C.J., 2000, Direct Observations of Skin-Bulk SST Variability, *Geophysical Research Letters*, 27, p. 1171-1174.

Nalli, N.R., Stowe, L.L.,2002, Aerosol correction for remotely sensed sea surface temperatures from the National Oceanic and Atmospheric Administration advanced very high resolution radiometer *J. Geophys. Res. Oceans*, 107(C10), 3172, doi:10.1029/2001JC001162.

Saunders, R.W., and Kriebel, K.T., 1988, An Improved Method for Detecting Clear Sky and Cloudy Radiances From Avhrr Data, *International Journal of Remote Sensing*, 9, p. 123-150.

Saunders, R., Matricardi, M., and Brunel, P., 1999, An Improved Fast Radiative Transfer Model for Assimilation of Satellite Radiance Observations, *Quarterly Journal of the Royal Meteorological Society*, 125, p. 1407-1425.

Simpson, J.J., Schmidt, A., and Harris, A., 1998, Improved Cloud Detection in Along Track Scanning Radiometer (ATSR) Data Over the Ocean, *Remote Sensing of Environment*, 66, p. 110

Tanré, D., Kaufman, Y.J., Herman, M., Mattoo, S., 1997, Remote sensing of aerosol properties over oceans using the MODIS/EOS spectral radiances, *J. Geophys. Res. Atmospheres*, 102 (D14), p. 16,971-16,988.

Vázquez-Cuervo, J., Armstrong, E.M., Harris, A., 2004, The effect of aerosols and clouds on the retrieval of infrared sea surface temperatures, *J. Climate*, 17 (20), p. 3,921-3,933.

Walton, C.C., Pichel, W.G., Sapper, J.F., May, D.A., 1998, The Development and Operational Application of Nonlinear Algorithms for the Measurement of Sea Surface Temperatures With the NOAA Polar-Orbiting Environmental Satellites, *J. Geophys. Res. Oceans*, 103 (C12), p. 27,999-28,012.

Waquet, F., Léon, J.-F., Goloub, P., Pelon, J., Tanré, D., Deuzé, J.-L., 2005, Maritime and dust aerosol retrieval from polarized and multispectral active and passive sensors, *J. Geophys. Res. Atmospheres*, 110 (D10S10).

Zavody, A.M., Mutlow, C.T., Llewellyn-Jones, D.T., 1995, A Radiative-Transfer Model for Sea-Surface Temperature Retrieval for the Along-Track Scanning Radiometer, *J. Geophys. Res. Oceans*, 100, p. 937-952.

Zavody, A.M., Mutlow, C.T., Llewellyn-Jones, D.T., 2000, Cloud Clearing Over the Ocean in the Processing of Data From the Along-Track Scanning Radiometer (ATSR), *Journal of Atmospheric and Oceanic Technology*, 17, p. 595-615.

Tables

Base altitude of aerosol layer / km	0		1		2		3	
Element of **k**	OPAC	Haywood	OPAC	Haywood	OPAC	Haywood	OPAC	Haywood
3.9 µm	-1.19	-1.14	-1.39	-1.28	-1.59	-1.41	-1.78	-1.55
8.7 µm	-0.46	-0.56	-1.16	-1.42	-1.97	-2.40	-2.82	-3.43
11 µm	-1.47	-1.11	-2.34	-1.99	-3.29	-2.97	-4.23	-3.97
12 µm	-0.96	-0.84	-1.83	-1.38	-2.84	-1.98	-3.89	-2.59

Table 1 Simulations of aerosol impact on BTs, **k** , in kelvin, for different base altitudes of the aerosol layer, for AOD = 0.5 at 10 µm, and for 0° satellite zenith angle. Results are given for two sets of aerosol characteristics, OPAC and Haywood (see main text for details). {*Complete tabulations for other configurations of factors are given in Appendix 2.*}

Base height of Saharan aerosol / km:	0		1		2		3	
	Bias	SDI	Bias	SDI	Bias	SDI	Bias	SDI
OPAC	-1.91	0.07	-2.52	0.23	-3.05	0.40	-3.49	0.54
Haywood	-1.25	-0.04	-2.27	0.33	-3.39	0.75	-4.54	1.20

Table 2 Bias in SST for 1 km layers of Saharan dust with bases at the indicated altitudes, based on simulations of the brightness temperature impact using OPAC and Haywood parameters. The bias is calculated for AOD at 10 µm equal to 0.25 and satellite zenith angle of 36°.

Figures

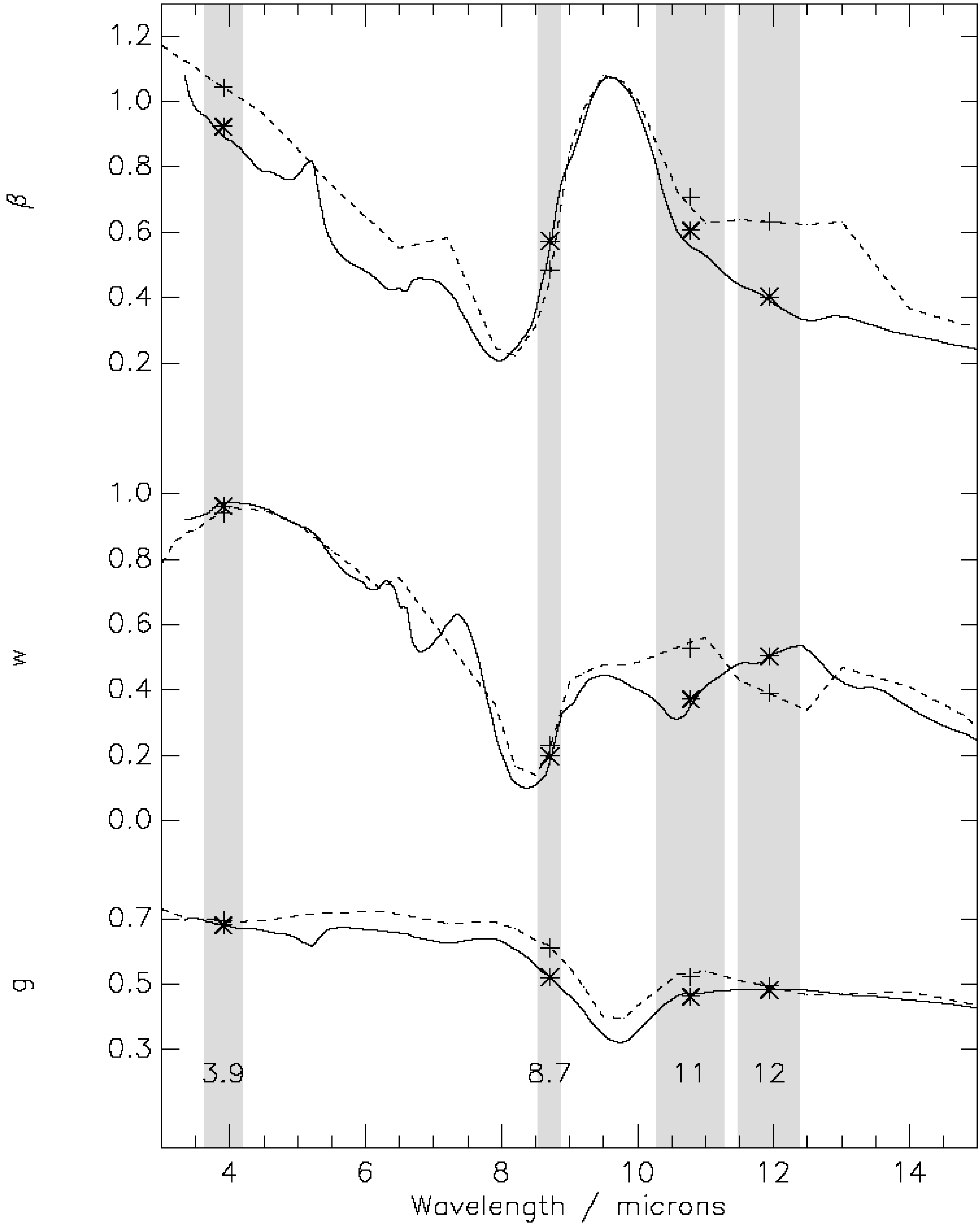

Figure 1. Variation of aerosol parameters with infrared wavelength. SEVIRI thermal window channels are also indicated. The absorption coefficient is normalized to 1.0 at 10 µm.

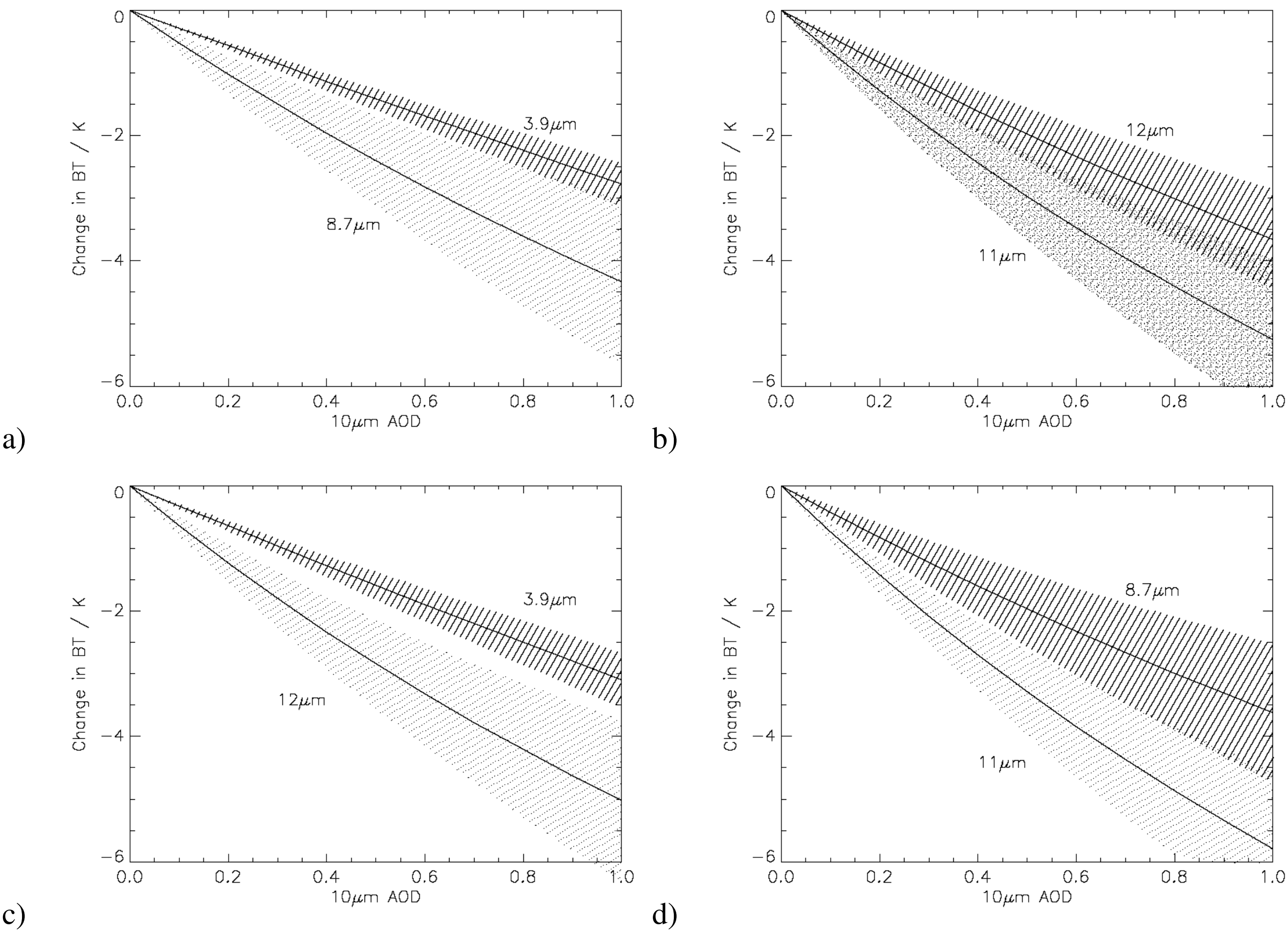

Figure 2. Mean (lines) and 1-σ range (shading) of change in BT versus AOD assuming a layer of aerosol evenly distributed between 2 and 3 km altitude. (a) and (b) use Haywood optical properties. (c) and (d) using OPAC dust parameters.

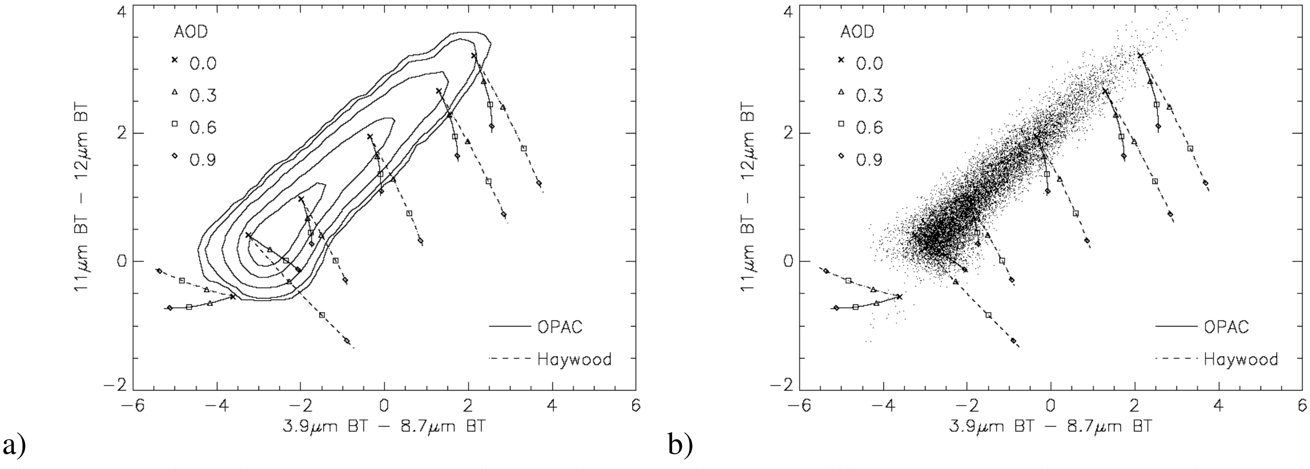

Figure 3. Trajectories with respect to increasing AOD in a BT-difference space, simulated using OPAC and Haywood parameters. (a) Contours surround: 99.9%, 99%, 95%, 80%, and 50% of points. (b) each simulation shown as an individual point.

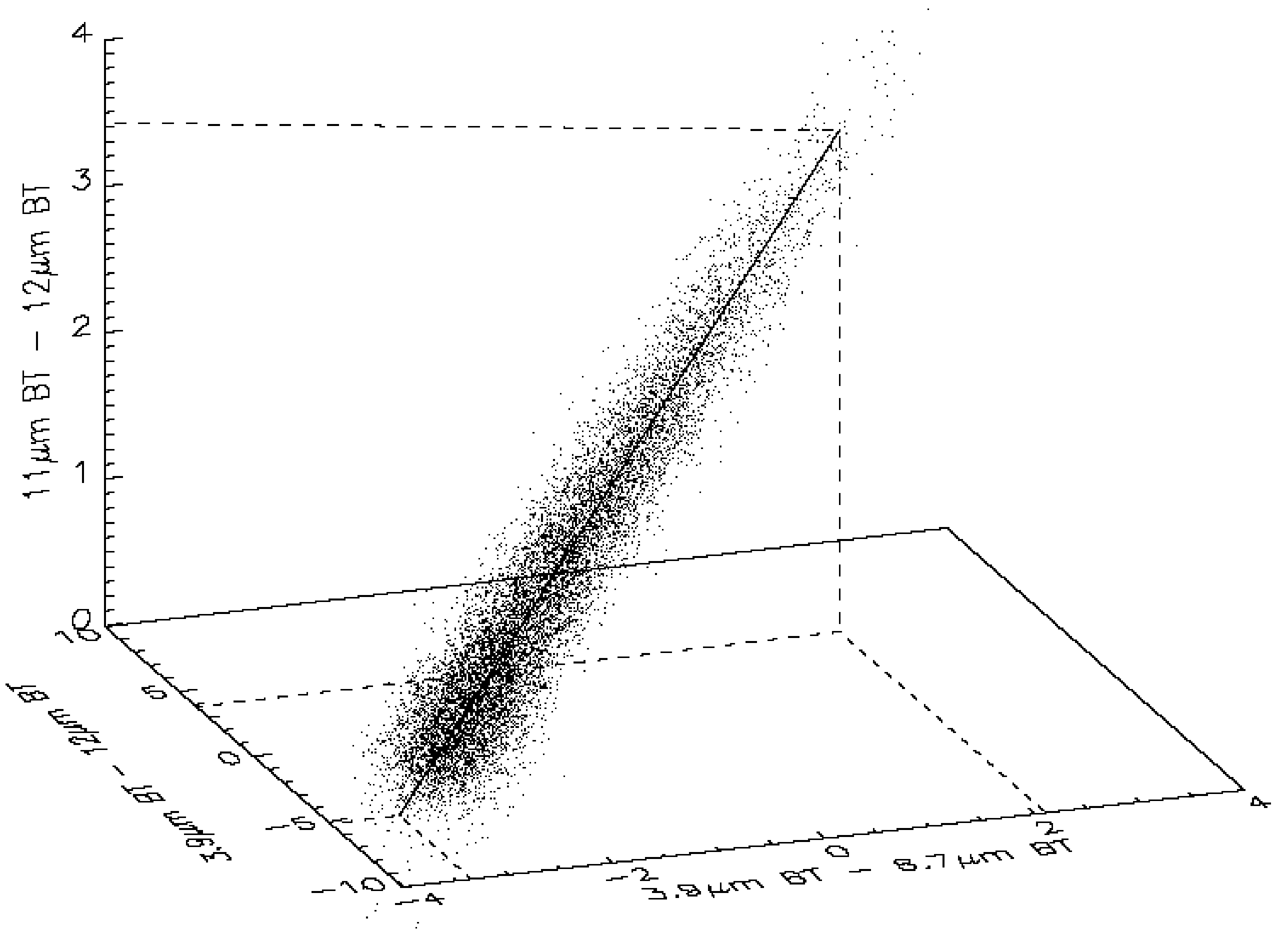

Figure 4. Location of aerosol-free simulations in a three-dimensional BT-difference space. The line is the axis of the first principal component of the points.

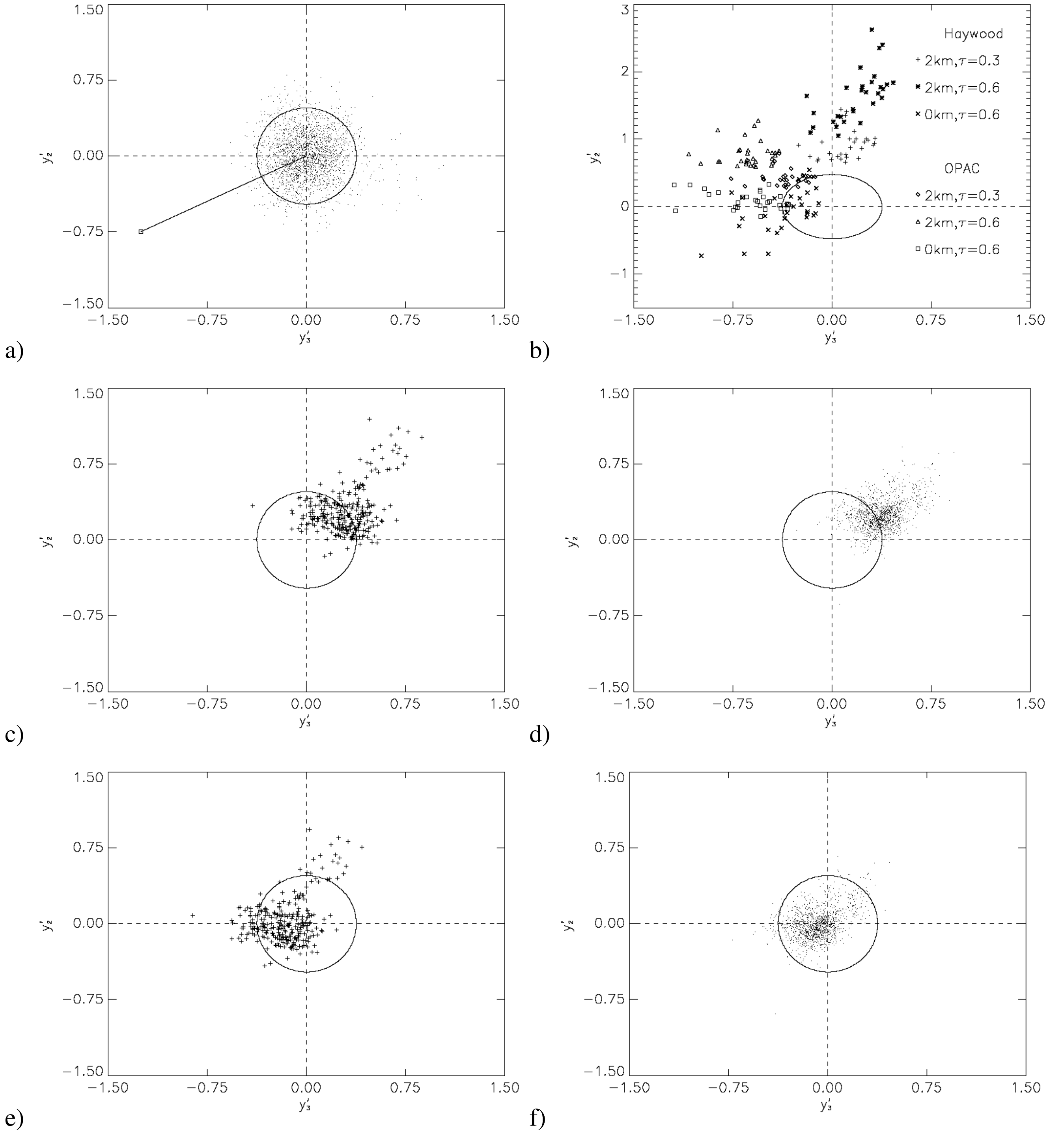
a)
b)
c)
d)
e)
f)
y'₂
y'₃
1.50
0.75
0.00
−0.75
−1.50
3
2
1
0
−1
Haywood
2km,τ=0.3
2km,τ=0.6
0km,τ=0.6
OPAC
2km,τ=0.3
2km,τ=0.6
0km,τ=0.6

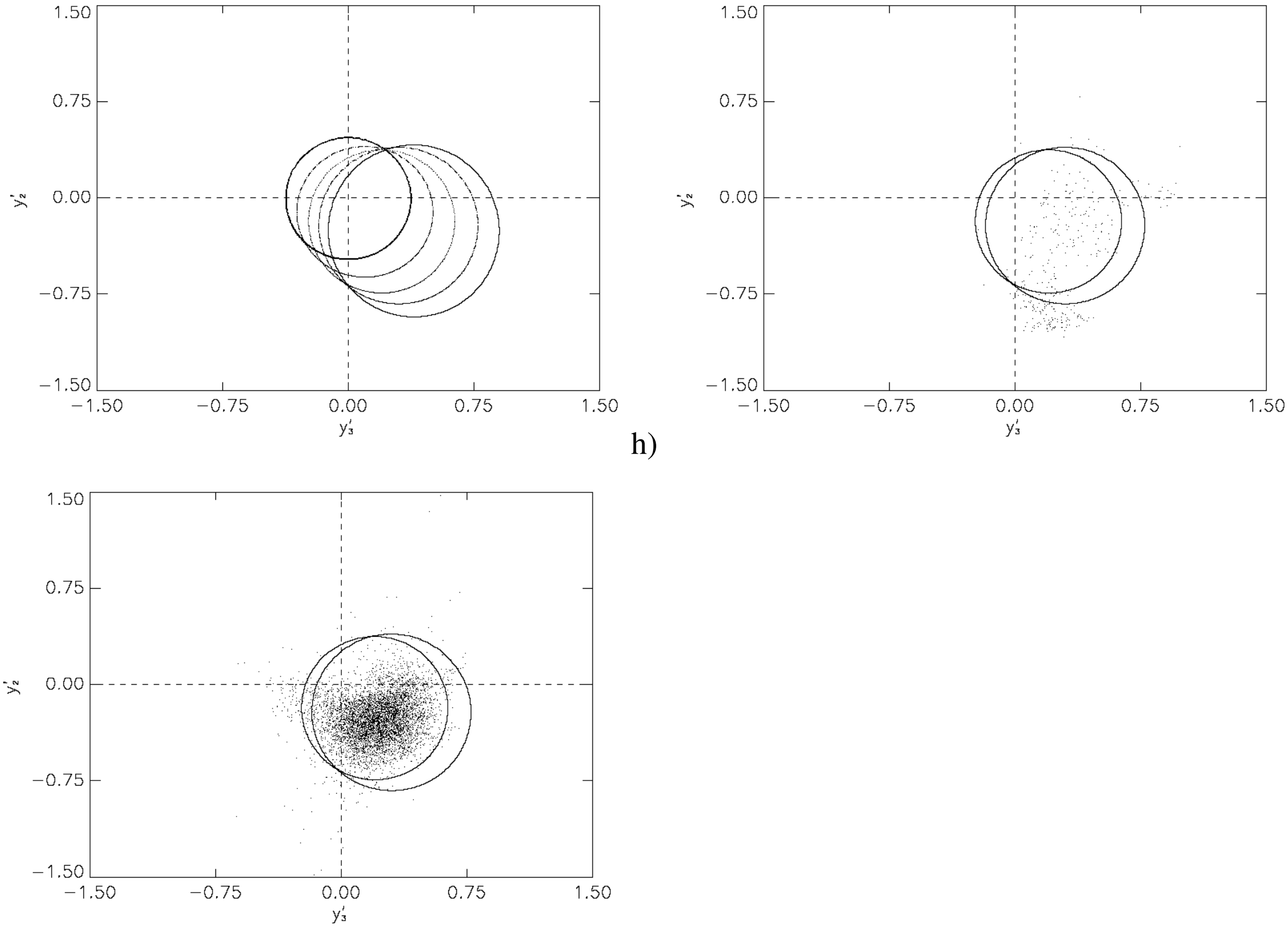

g)

h)

i)

Figure 5. Scatter plots of the weights of the second and third principal components of BTs in a three-dimensional BT-difference space. (a) Simulated aerosol-free BTs. The ellipse is the 2σ threshold. The square symbol represents a hypothetical point that lies outside the ellipse and is detectable. (b) Simulated dust-affected BTs. The ellipse is as in (a), but the aerosol-free points are not shown. (c) SEVIRI observations from the Interactive Test data, selected as being aerosol-free, and with a satellite zenith angle of less than 30°. (d) as (c), but using observations from the MDB. (e) and (f) as (c) and (d), but having adjusted the simulations of the 8.7 μm channel by -0.6 K prior to defining the principal components. (g) Ellipses as in (a), but for increasing satellite zenith angles: thick solid line, 0°; dashed, 36.8°; dotted, 48.2°; dot-dashed, 55.2°; and thin solid, 60°. (h) and (i) as (c) and (d), but for SEVIRI observations between 48° and 56°, with the ellipses for 48.2° and 55.2° also drawn.

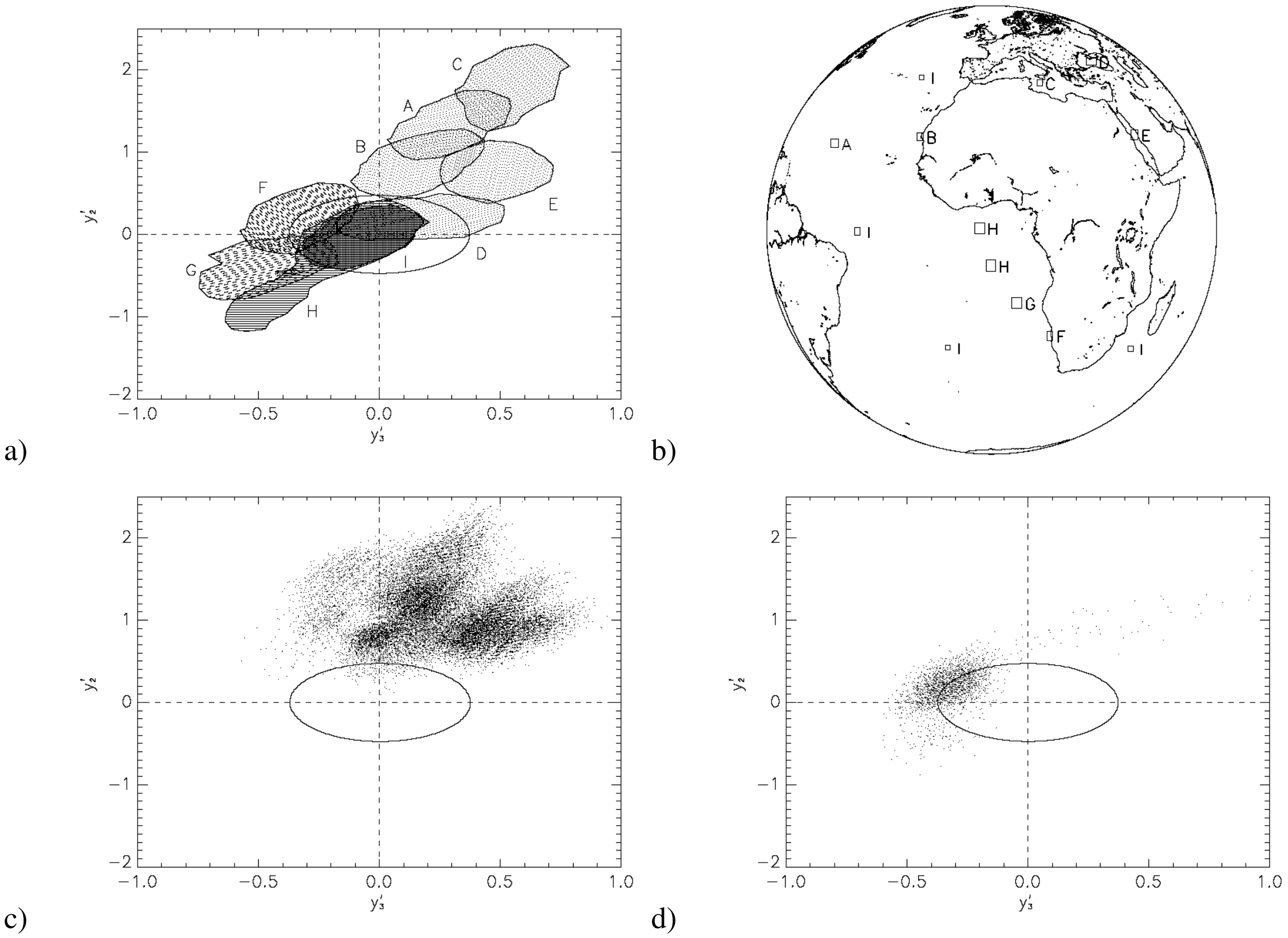

Figure 6. Actual SEVIRI data plotted in PC plane, any pixels flagged as cloud by the SEVIRI cloud mask have been excluded. (a) Contours showing regions of PC plane corresponding to selected areas of SEVIRI imagery. (b) Location in SEVIRI FOV of regions shown in (a). (c) Scatter plot of pixels from many locations manually identified as aerosol. Data comes from 30 locations in the Atlantic Ocean, Mediterranean, and Red Sea for six days in the period 20th to 26th July 2005. (d) Scatter plot of pixels in region F.

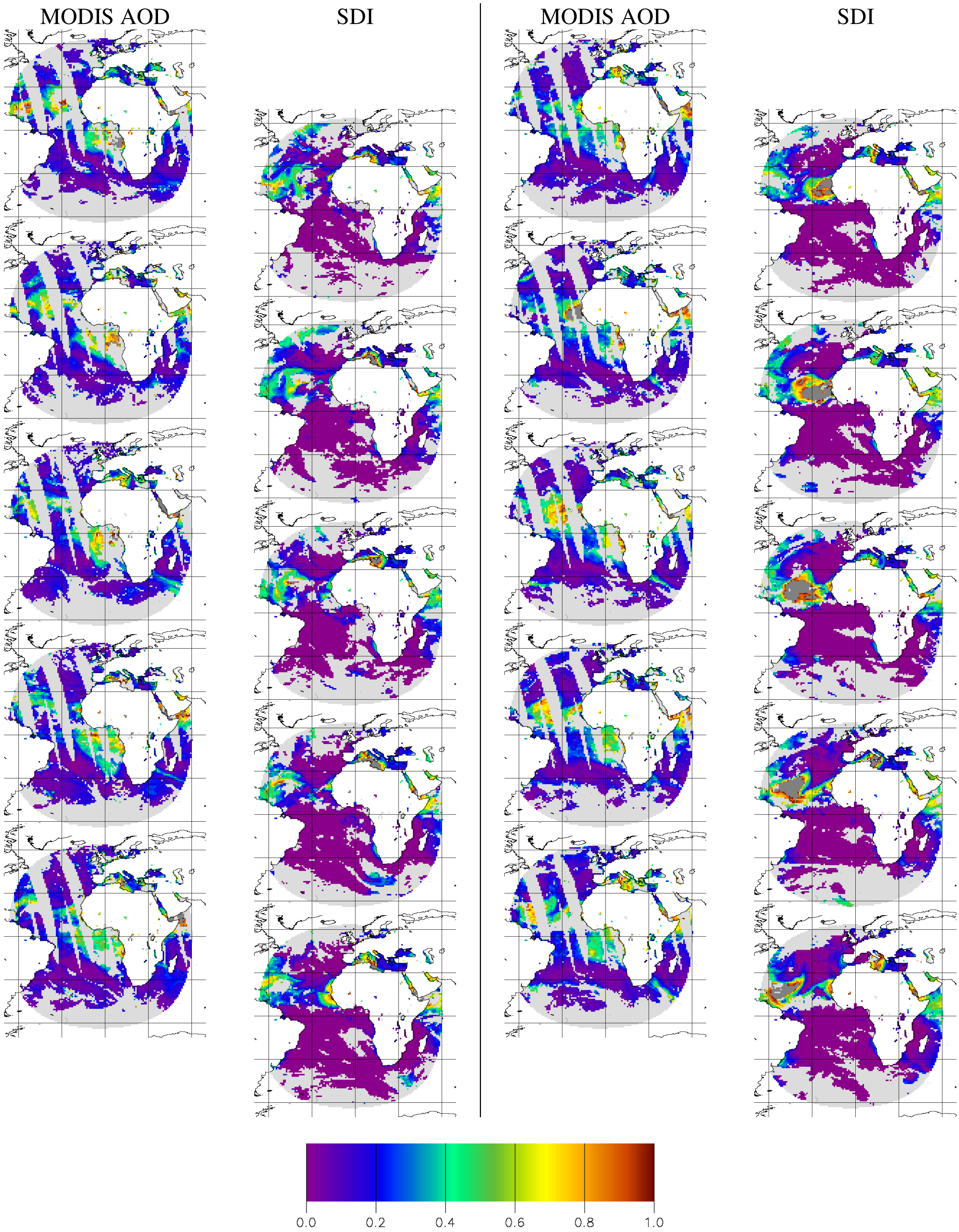

Figure 7. Comparison of MODIS AOD and SDI. MODIS columns show daily average AOD on 1° grid. Cells corresponding to land masses or MSG SZA > 75° have been excluded. Top to bottom images correspond to dates 24/7/2005 though 28/7/2005 for first column, and 29/7/2005 though 2/8/2005 for second column. SDI columns show nightly average MSG aerosol index (y_2') on a 1° grid. Negative aerosol index is shown as zero.

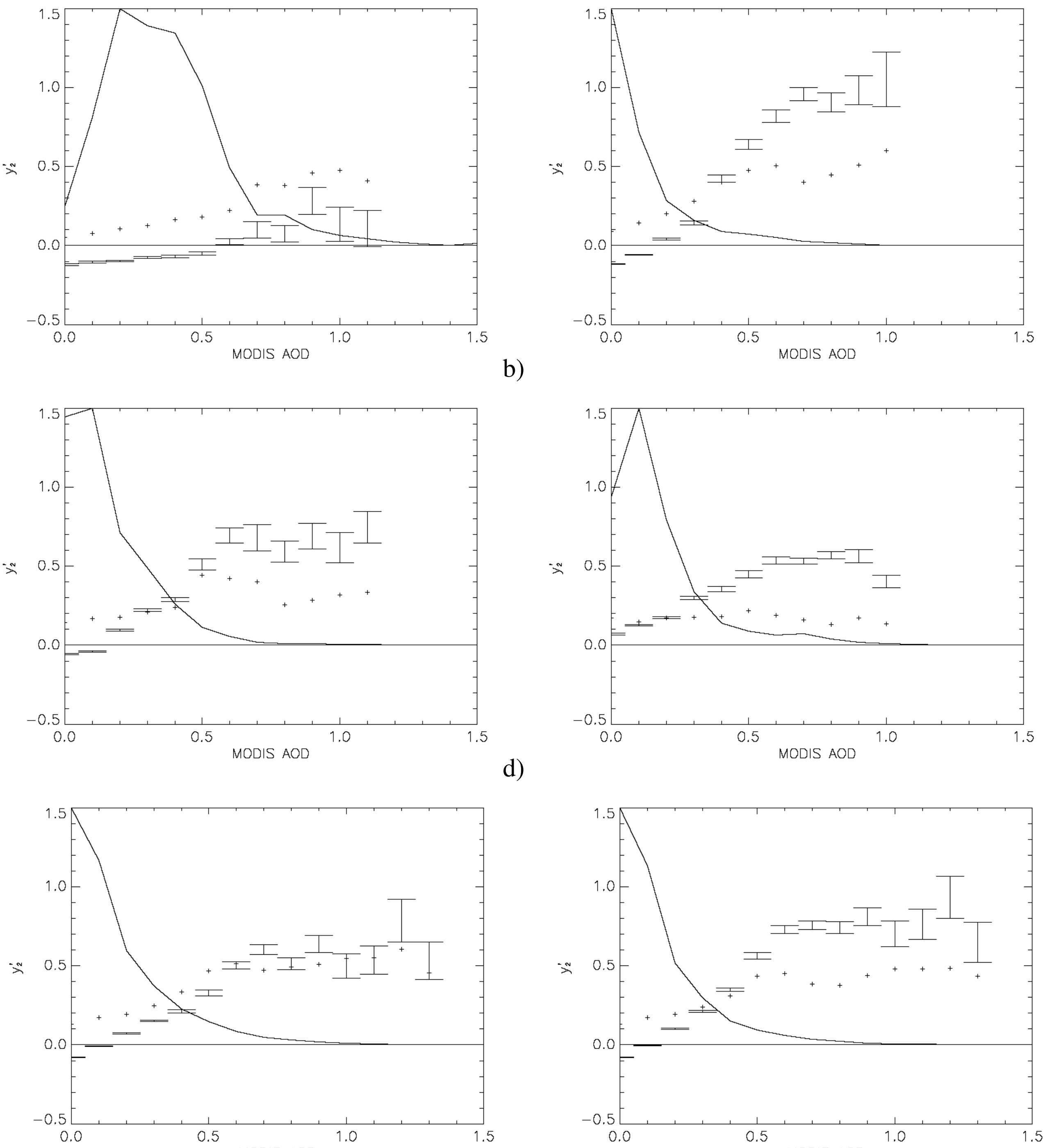

a) b) c) d) e) f)

Figure 8. Mean and standard deviation of SDI against MODIS AOD. Results have been binned in intervals of 0.1 MODIS AOD. The “error bar” for each bin shows the range of the mean SDI minus one standard error to the mean SDI plus one standard error. Crosses show the standard deviation of SDI in each bin. The solid line is the frequency distribution of MODIS AOD normalized such that the peak distribution is full scale on the vertical axis. (a) MSG SZA 0° to 24° (b) SZA 24° to 48° (c) SZA 48° to 60° (d) SZA 60° to 72° (e) SZA 0° to 72° (f) SZA 24° to 72°

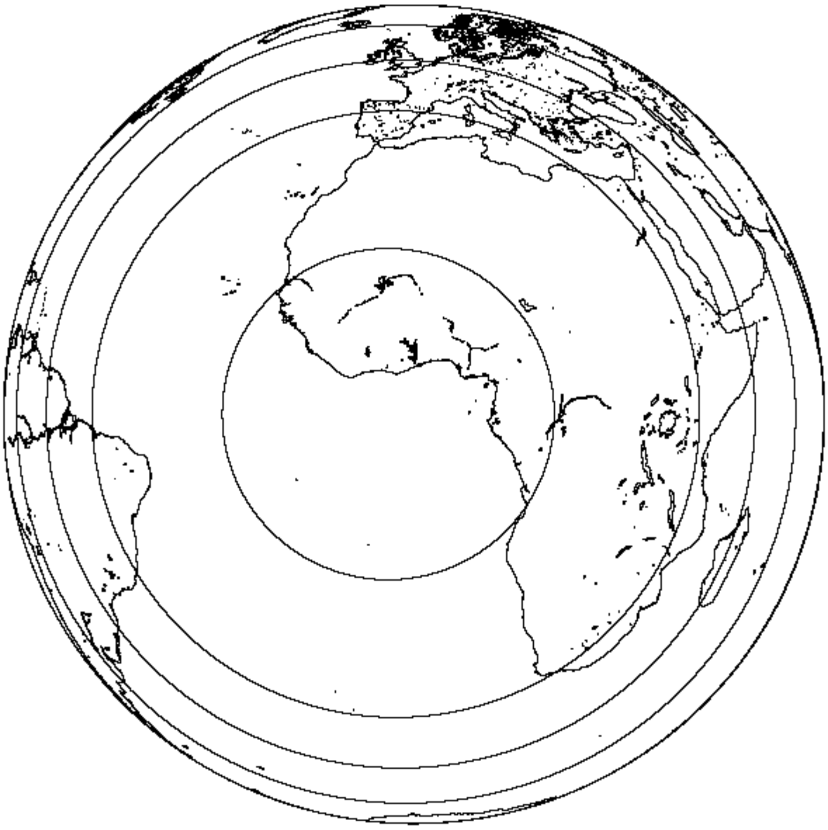

Figure 9. Satellite zenith angle shown on SEVIRI FOV. From inside to outside, contours correspond to SZA of 24°, 48°, 60°, 72°, and edge of globe.

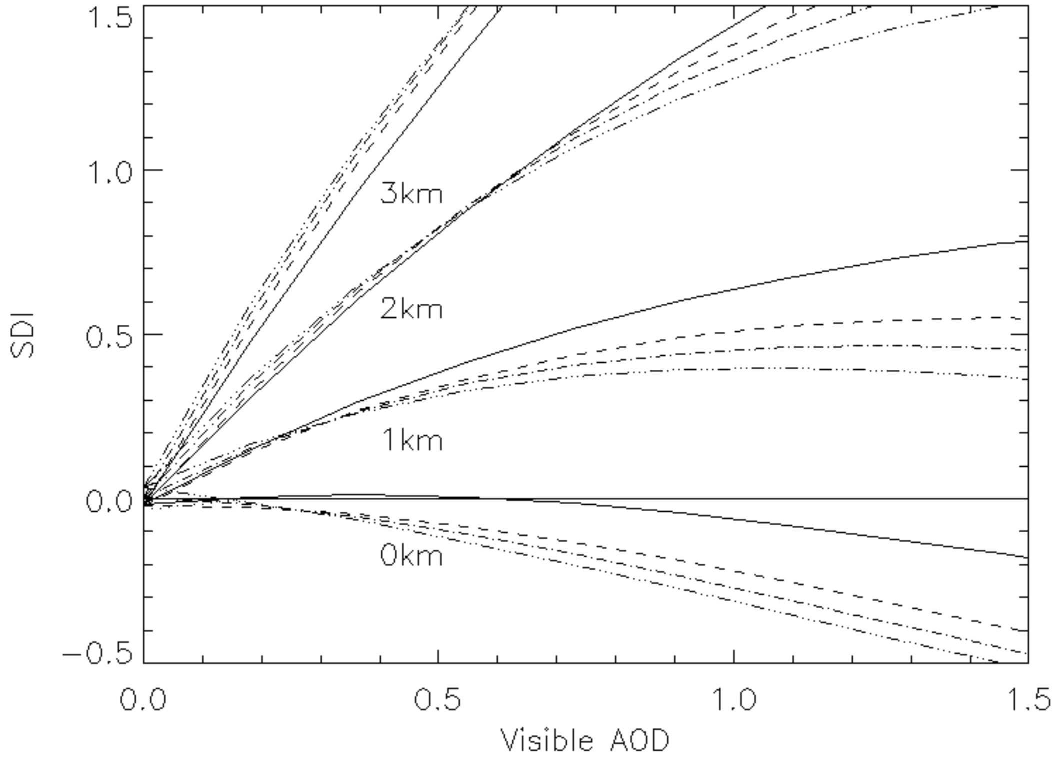

Figure 10. SDI against visible AOD for SAFREE simulations using Haywood parameters at different zenith angle and aerosol base height. Zenith angles are: solid line, 0°; dotted, 48.2°; dashed, 55.2°; dot-dashed, 60.0°

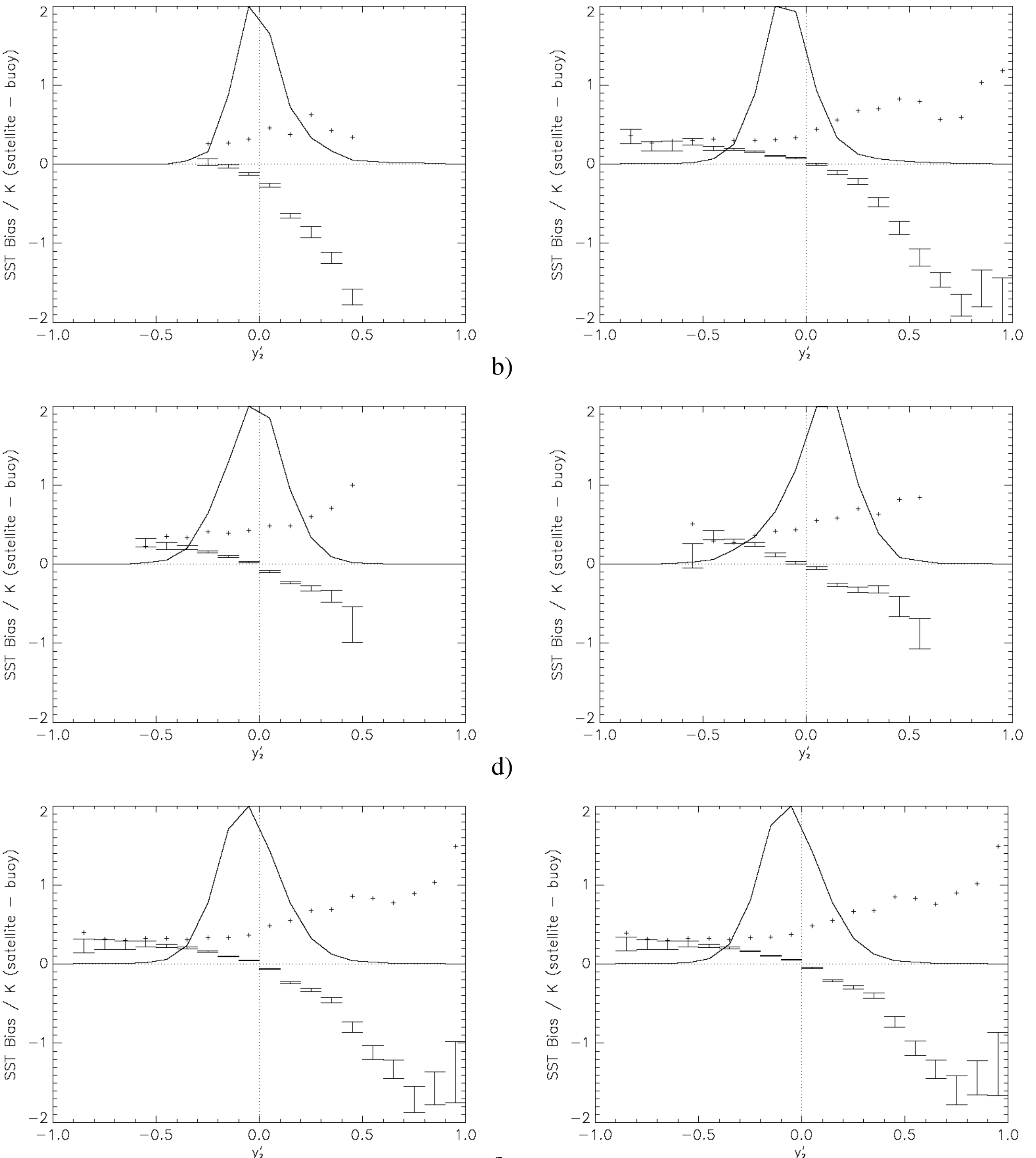

a) b) c) d) e) f)

Figure 11. Bias and standard deviation of SEVIRI retrievals of SST compared to *in situ* observations, against the index of Saharan dust. Error bars show mean bias with standard error. Crosses show standard deviation of error. Line shows frequency distribution of SDI. (a) SZA 0° to 24° (b) SZA 24° to 48° (c) SZA 48° to 60° (d) SZA 60° to 72° (e) SZA 0° to 72° (f) SZA 24° to 72°

List of table captions

Table 1 Simulations of aerosol impact on BTs, **k** , in kelvin, for different base altitudes of the aerosol layer, for AOD = 0.5 at 10 μm, and for 0° satellite zenith angle. Results are given for two sets of aerosol characteristics, OPAC and Haywood (see main text for details). {*Complete tabulations for other configurations of factors are given in Appendix 2.*}

Table 2 Bias in SST for 1 km layers of Saharan dust with bases at the indicated altitudes, based on simulations of the brightness temperature impact using OPAC and Haywood parameters. The bias is calculated for AOD at 10 μm equal to 0.25 and satellite zenith angle of 36°.

List of figure captions

Figure 1. Variation of aerosol parameters with infrared wavelength. SEVIRI thermal window channels are also indicated. The absorption coefficient is normalized to 1.0 at 10 μm.

Figure 2. Mean (lines) and 1-σ range (shading) of change in BT versus AOD assuming a layer of aerosol evenly distributed between 2 and 3 km altitude. (a) and (b) use Haywood optical properties. (c) and (d) using OPAC dust parameters.

Figure 3. Trajectories with respect to increasing AOD in a BT-difference space, simulated using OPAC and Haywood parameters. (a) Contours surround: 99.9%, 99%, 95%, 80%, and 50% of points. (b) each simulation shown as an individual point.

Figure 4. Location of aerosol-free simulations in a three-dimensional BT-difference space. The line is the axis of the first principal component of the points.

Figure 5. Scatter plots of the weights of the second and third principal components of BTs in a three-dimensional BT-difference space. (a) Simulated aerosol-free BTs. The ellipse is the 2σ threshold. The square symbol represents a hypothetical point that lies outside the ellipse and is detectable. (b) Simulated dust-affected BTs. The ellipse is as in (a), but the aerosol-free points are not shown. (c) SEVIRI observations from the Interactive Test data, selected as being aerosol-free, and with a satellite zenith angle of less than 30°. (d) as (c), but using observations from the MDB. (e) and (f) as (c) and (d), but having adjusted the simulations of the 8.7 μm channel by -0.6 K prior to defining the principal components. (g) Ellipses as in (a), but for increasing satellite zenith angles: thick solid line, 0°; dashed, 36.8°; dotted, 48.2°; dot-dashed, 55.2°; and thin solid, 60°. (h) and (i) as (c) and (d), but for SEVIRI observations between 48° and 56°, with the ellipses for 48.2° and 55.2° also drawn.

Figure 6. Actual SEVIRI data plotted in PC plane, any pixels flagged as cloud by the SEVIRI cloud mask have been excluded. (a) Contours showing regions of PC plane corresponding to selected areas of SEVIRI imagery. (b) Location in SEVIRI FOV of regions shown in (a). (c) Scatter plot of pixels from many locations manually identified as aerosol. Data comes from 30 locations in the Atlantic Ocean, Mediterranean, and Red Sea for six days in the period 20th to 26th July 2005. (d) Scatter plot of pixels in region F.

Figure 7. Comparison of MODIS AOD and SDI. MODIS columns show daily average AOD on 1° grid. Cells corresponding to land masses or MSG SZA > 75° have been excluded. Top to bottom images correspond to dates 24/7/2005 though 28/7/2005 for first column, and 29/7/2005 though 2/8/2005 for second column. SDI columns show nightly average MSG aerosol index (y_2') on a 1° grid. Negative aerosol index is shown as zero.

Figure 8. Mean and standard deviation of SDI against MODIS AOD. Results have been binned in intervals of 0.1 MODIS AOD. The “error bar” for each bin shows the range of the mean SDI minus one standard error to the mean SDI plus one standard error. Crosses show the standard deviation of SDI in each bin. The solid line is the frequency distribution of MODIS AOD normalized such that the peak distribution is full scale on the vertical axis. (a) MSG SZA 0° to 24° (b) SZA 24° to 48° (c) SZA 48° to 60° (d) SZA 60° to 72° (e) SZA 0° to 72° (f) SZA 24° to 72°.

Figure 9. Satellite zenith angle shown on SEVIRI FOV. From inside to outside, contours correspond to SZA of 24°, 48°, 60°, 72°, and edge of globe.

Figure 10. SDI against visible AOD for SAFREE simulations using Haywood parameters at different zenith angle and aerosol base height. Zenith angles are: solid line, 0°; dotted, 48.2°; dashed, 55.2°; dot-dashed, 60.0°

Figure 11. Bias and standard deviation of SEVIRI retrievals of SST compared to *in situ* observations, against the index of Saharan dust. Error bars show mean bias with standard error. Crosses show standard deviation of error. Line shows frequency distribution of SDI. (a) SZA 0° to 24° (b) SZA 24° to 48° (c) SZA 48° to 60° (d) SZA 60° to 72° (e) SZA 0° to 72° (f) SZA 24° to 72°

Appendix 1 RTTOV8_IRS – A Version of RTTOV8 which implements the delta-Eddington approximation for scattering at infra-red wavelengths.

A1 Introduction

This document describes IRSCATT, an experimental version of RTTOV8 where the delta-Eddington code for calculating microwave radiances in the presence of precipitating clouds has been modified to work at infrared wavelengths. Currently IRSCATT only supports forward model calculations. Tanglent linear, adjoint and K codes have not been implemented.

A2 Delta-Eddington approximation

The delta-Eddington approximation is actually a collection of three approximations: Eddington's first and second approximations, and the delta-approximation. Eddington’s first approximation allows an analytical solution to the radiative transfer equation in a scattering medium by assuming a simple form for the radiance field and scattering phase function. Eddington’s second approximation improves the accuracy by calculating the effect of extinction/absorption and scattering seperatly. The delta-approximation also improves the accuracy by treating radiation which is scattered directly forward as unscattered radiation.

The development of the delta-Eddington approximation and its application to microwave radiances for RTTOV8 has already been described in detail by Bauer [2002] and Saunders et al [2005]. Therefore only a brief summary and equations directly relevant to its implementation in RTTOV8 will be given here.

A2.1 Eddington approximation

The radiative transfer equation for a plane-parallel atmosphere can be written as:

$$\begin{aligned} \mu\frac{dL(z;\mu)}{\beta dz} &= L(z;\mu) - J(z;\mu) \quad \text{(upward)} \\ -\mu\frac{dL(z;\mu)}{\beta dz} &= L(z;\mu) - J(z;\mu) \quad \text{(downward)} \end{aligned} \qquad \text{(A1)}$$

where $L(z;\mu)$ is the radiance at altitude z, zenith angle $\theta = \cos^{-1}\mu$, and assuming azimuth angle can be neglected. The volume extinction coefficient, $\beta = \beta_{sct} + \beta_{abs}$, comprises both scattering and absorption components. The source function, $J(z;\mu)$, represents contributions to the radiance from scattering and emission and is given by:

$$J(z;\mu) = \frac{\omega}{2}\int_{-1}^{1} L(z;\mu')P(\mu;\mu')d\mu' + (1-\omega)B[T(z)] \qquad \text{(A2)}$$

where the single scattering albedo, $\omega = \beta_{sct} / \beta$, is the fraction of radiation scattered rather than absorbed. The phase function, $P(\mu;\mu')$, represents the proportion of radiation scattered into the direction μ, from direction μ'. $B[T(z)]$ is the blackbody equivalent or Planck radiance corresponding to temperature T. For general $L(z;\mu)$ and $J(z;\mu)$, Eq. A1 can only be solved using computationally expensive numerical methods. However; the Eddington approximation assumes a simple first order representation of the radiance field and phase function which allows an analytical solution. The functions used are:

$$\begin{aligned} L(z;\mu) &= L_0(z) + \mu L_1(z) \\ P(\mu;\mu') &= 1 + 3g\mu\mu' \end{aligned} \qquad \text{(A3)}$$

where g, the asymmetry parameter, is the first moment of the phase function. L_0 and L_1 represent the isotropic and anisotropic components of the radiance field. Substituting Eqs. A3 into Eq. A1 gives two mixed differential equations:

$$\begin{aligned}\frac{dL_1(z)}{dz} &= -3\beta(z)[1-\omega(z)]\{L_0(z)-B[T(z)]\} \\ \frac{dL_0(z)}{dz} &= -\beta(z)[1-\omega(z)g(z)]L_1(z)\end{aligned} \tag{A4}$$

If a thin layer of atmosphere is considered, such that the single scattering properties β, ω, and g can be assumed constant, the general solution to Eq. A4 is:

$$L_0(z') = D^+\exp(\Lambda z') + D^-\exp(\Lambda z') + B[T_0] + B_1 z' \tag{A5}$$

where:

$$\Lambda^2 = 3\beta^2(1-\omega)(1-\omega g) \tag{A6}$$

Here it has been assumed that the blackbody radiance varies linearly with altitude within the layer (z'). The coefficients $D^{\pm}$ are found from the boundary conditions: space background at the top of the atmosphere, surface emission and reflection at the bottom, and flux continuity at the layer boundaries. These are expressed in Eq. A7 below:

$$\begin{aligned}&\left(L_0 - \frac{\partial L_0}{h\partial z}\right)_{z=z^*} = B(2.7) \\ &\left(L_0 + \frac{\partial L_0}{h\partial z}\right)_{z=0} = \bar{\varepsilon}B(T) + (1-\bar{\varepsilon})\left(L_0 - \frac{\partial L_0}{h\partial z}\right)_{z=0} \\ &\left(L_0 \pm \frac{\partial L_0}{h\partial z}\right)^{j}_{z=z_i} = \left(L_0 \mp \frac{\partial L_0}{h\partial z}\right)^{j+1}_{z=z_i}\end{aligned} \tag{A7}$$

where:

$$\begin{aligned}h &= \frac{3\beta}{2}(1-\omega g) \\ \bar{\varepsilon} &= 2\int_0^1 \varepsilon(\mu)\mu d\mu\end{aligned} \tag{A8}$$

$\varepsilon(\mu)$ is the angular dependent surface emissivity and $\bar{\varepsilon}$ is the hemispheric emissivity.

Inserting Eq. A5 into Eqs. A7 produces a set of linear equations of the form $AD^{\pm} = B$. These can be solved to determine the Eddington radiance as defined in Eq. A3. However; the accuracy can be significantly improved using Eddington's second approximation. This involves substituting the Eddington radiances back into the source function Eq. A2

$$J(z;\mu) = (1-\omega)B[T(z)] + \omega[L_0(z) + g\mu L_1(z)] \tag{A9}$$

and integrating through the atmosphere. This effectively means that extinction and emission are calculated independently of Eddington's first approximation. Only scattering into the line of sight depends on the first order representation of the radiance field and phase function.

A2.2 Delta approximation

The delta approximation compensates for some of the accuracy lost by only considering the first moment of the phase function in Eq. A3. The Eddington phase function is a smoothly varying function of μ, while in reality phase functions have a strong forward peak. Delta scaling of the single scattering properties approximates the forward peak with a delta-function, scattering into this direction is mathematically equivalent to not being scattered, and the resulting phase function more accurately matches the model. The delta-scaled single scattering properties are:

$$g' = \frac{g}{1+g}, \quad \omega' = \frac{(1-g)^2\omega}{1-g^2\omega}, \quad \beta' = (1-\omega g^2)\beta \tag{A10}$$

These values are used in place of β, ω, and g in all the previous equations.

A2.3 Combining single scattering properties

When performing radiative transfer calculations it is often the case that multiple components contribute to the single scattering properties. These components can include different aerosol species, hydrometeors (cloud liquid water, cloud ice water, rain, etc.), and 'clear-sky' with no scattering ($\beta = \beta_{abs}$, $\omega = 0$). The single scattering properties from multiple components can be combined using the following equations:

$$\begin{aligned}
\beta &= \sum \beta_i \\
\omega &= \frac{\sum \omega_i \beta_i}{\sum \beta_i} \qquad \text{(A11)} \\
g &= \frac{\sum g_i \omega_i \beta_i}{\sum \omega_i \beta_i}
\end{aligned}$$

where the subscript i refers to the different components.

A3 Original implementation for microwave frequencies

The RTTOV_SCATT code in RTTOV8 calculates scattering effects at microwave frequencies using the delta-Eddington approximation. It takes as input a standard RTTOV profile (temperature, water vapour, and ozone on 43 fixed pressure levels and 2m values), and a 'cloud profile' which comprises temperature, cloud liquid water (kg/kg), cloud ice water (kg/kg), rain (kg/m^2), and solid precipitation (kg/m^2) on user defined pressure levels (both the average pressure of each layer and the pressure of the layer interfaces must be supplied).

Table A1. outlines the hierarchy of function calls in the RTTOV_SCATT code. Details, with reference to the equations in Section A2, are given below.

1. RTTOV_DIRECT is called using the 43-level input profile in order to determine the optical depth of each atmospheric layer in the absence of scattering.
2. RTTOV_INISCATT converts the optical depths on RTTOV levels to extinction coefficient on the user-defined pressure levels.
   It also converts the input cloud water/rain profiles to internally used units, and calculates the hemispheric surface emissivity (Eq. A8)
3. RTTOV_MIEPROC generates profiles of single scattering properties from the input profile of cloud liquid water, ice water, rain, and solid precipitation; and a sensor specific coefficient file. These profiles are combined with the clear-sky extinction profile (which by definition has $\omega = 0$) using Eq. A11
4. RTTOV_INIEDD calculates the remaining (simple) layer dependant variables: B_0 and B_1 for Eq. A5; performs delta-scaling of the single scattering properties (Eq. A10); and calculates the layer transmission ($\exp(-\delta)$ where $d\delta = \beta dz / \mu$)), Λ (Eq. A6), and h (Eq. A8).
5. RTTOV_BOUNDARYCONDITIONS solves Eq. A7 to determine the coefficients $D^{\pm}$
6. RTTOV_INTEGRATESOURCE integrates the source term (Eq. A9) for each layer.
7. Finally RTTOV_EDDINGTON integrates the radiative transfer equation (Eq. A1) using the source term calculations from RTTOV_INTEGRATESOURCE.

A4 Implementation at infrared frequencies

The IRSCATT code implements delta-Eddington scattering at infrared frequencies. Table A2 outlines the hierarchy of function calls. Each function replaces a similarly named RTTOV_SCATT function with the changes described below.

A4.1 Rayleigh-Jeans approximation

The RTTOV_SCATT code assumed the Rayleigh-Jeans approximation and performed all scattering calculations in temperature space rather than radiance space. At infrared frequencies the Rayleigh-Jeans

approximation is no longer valid and the calculations must be performed in radiance space. The first file affected by this change is IRSCATT_INISCATT where B_0, B_1, and B_n are now radiances, this means they must be calculated per channel, rather than per profile. This change from per-profile to per-channel requires minor changes to all the subsequent files. Similarly the surface radiance calculated in IRSCATT_EDDINGTON is now a true radiance, rather than a temperature, this also required minor changes to the calculation of $D^{\pm}$ in IRSCSATT_BOUNDARYCONDITIONS.
Finally the BT to radiance conversion has been replaced with a radiance to BT conversion in the main routine IRSCATT_IRSCATT.

A4.2 Source terms without scattering

In layers where no scattering occurs (i.e. $\omega = 0$), RTTOV_EDDINGTION sets the source terms to $J^{\pm} = B_0(1-\tau)$ where τ is the transmission of the layer, i.e. the layer is assumed to be thermally emitting a the temperature of the lower boundary of the layer. It was found that running IRSCATT with a clear-sky profile (i.e. no scattering) gave results ~0.1K different to the standard RTTOV8 program. In standard RTTOV8 the average radiance from the upper and lower boundaries is used, therefore IRSCATT_EDDINGTON sets the source terms to $J^{\pm} = (B_0 + B_n)(1-\tau)/2$. This reduced the clear-sky differences to ~0.02K.

A4.3 Input Profile

RTTOV_SCATT takes two main structures as input: a standard 43-level RTTOV profile and a 'cloud-profile' containing temperature, pressure, and hydrometeor concentration on user-defined pressure levels. IRSCATT takes the same two structures (but currently ignores the hydrometeor data in the 'cloud-profile') and an additional structure (shown in Table A3) on the same pressure levels as the 'cloud-profile' which contains profiles of extinction coefficient for any number of scattering components. This new structure is currently referred to as profile_aerosol_type. However; it could also be used to represent clouds etc. Aerosol concentrations are given in terms of the extinction coefficient (km^{-1}) at a wavelength of 10 microns, rather than kg/kg or kg/m^2 as used for the cloud-profile.

A4.4 Single Scattering Properties

Previously the function RTTOV_MIEPROC calculated the single scattering properties for each species of hydrometeor from the input cloud profile and a sensor specific coefficient file. These were then combined with the clear-sky extinction to give a single set of single scattering properties for each atmospheric layer.
In IRSCATT the input aerosol profile is given in terms of the extinction coefficient (km^{-1}) at a wavelength of 10 microns, so it is only necessary to convert this to the wavelenghts of the the instrument's channels and retrieve the single scattering albedo and assymetry parameter from lookup tables.

Aerosol optical properties are read from OPAC [Hess et al, 1998] data files using the routine IRSCATT_READOPAC and returned in a structure described in Table A4. Optical properties are automatically interpolated to the central wavenumber of each channel.

NOTE– The optical properties of some of the aerosols in the OPAC database depend on relative humidity. IRSCATT does not currently support these aerosols. If a relative humidity dependant aerosol is used, IRSCATT will use the aerosol properties attributed to a relative humidity of 0%.

4.5 Additional Routines

The IRSCATT package includes five additional routines not shown in Table A2. These are:

IRSCATT_CONST

Defines constants for IRSCATT. Currently the only constants defined are lookup tables of single scattering properties taken from LOWTRAN-7. As IRSCATT now uses the OPAC database this file is obselete.

IRSCATT_INTEXLIN

Performs linear interpolation of a profile to a new altitude grid.

IRSCATT_PPMV2RELHUM

Converts an input water vapour profile in ppmv to relative humidity. Part of the incomplete code to support relative humidity dependent aerosols.

IRSCATT_READOPAC

Reads the OPAC database and generates optical property lookup tables for the current RTTOV instrument

IRSCATT_TYPES

Defines additional datatypes used by IRSCATT

A5 References for Appendices

Bauer, P., 2002, Microwave radiative transfer modeling in clouds and precipitation, Part I: Model description. Satellite Application Facility for Numerical Weather Prediction, NWPSAF-EC-TR-005.

Hess, M., Koepke, P., Schult, I., 1998, Optical Properties of Aerosols and clouds: The software package OPAC, *Bull. Am. Met. Soc.*, 79, p. 831-844.

Saunders, R., Brunel, P., English, S., Bauer, P., O'Keeffe, U., Francis, P., Rayer, R., 2005, RTTOV-8 – Science and validation report. *Satellite Application Facility for Numerical Weather Prediction*, NWPSAF-MO-TV-007

RTTOV_SCATT.F90

- **RTTOV_DIRECT.F90**
  - Standard RTTOV model. Calculates level to space transmittances on standard RTTOV levels and ToA radiances.
- **RTTOV_INISCATT.F90**
  - Calculates temperature at model layer boundaries
  - Calculates thickness of each model layer
  - Interpolate optical depths (hPa^{-1}) from RTTOV levels to model levels
  - Convert optical depths from hPa^{-1} to km^{-1}
  - Convert unit of input rain profiles etc.
  - **RTTOV_MIEPROC.F90**
    - Calculates scattering parameters (β,ω,g) from coefficient file and input rain profile.
  - **RTTOV_INIEDD.F90**
    - Calculates some initial parameters for the delta-Eddington model from the single scattering properties and temperature profile.
  - Calculate surface emissivity integrated over π
- **RTTOV_EDDINGTON.F90**
  - Calculates input BTs at surface, ToA, and layer boundaries.
  - **RTTOV_BOUNDARYCONDITIONS.F90**
    - Solves system of linear equations to obtain $D^{\pm}$
  - **RTTOV_INTEGRATESOURCE.F90**
    - Integrates the source function to determine the up/downwelling radiances from each layer
  - Integrates BTs to get ToA BT
- Convert BTs to radiances

Table A1 Structure of RTTOV_SCATT program.

- **IRSCATT_IRSCATT.F90**
  - **RTTOV_DIRECT.F90**
    - Standard RTTOV model. Calculates level to space transmittances on standard RTTOV levels and ToA radiances.
  - **IRSCATT_INISCATT.F90**
    - Check input model pressure levels
    - Call RTTOV_SETGEOMETRY
    - Calculates temperature at model layer boundaries
    - Calculates thickness of each model layer
    - Interpolate optical thickness (in hPa^{-1}) from RTTOV levels to model levels
    - Convert optical thickness from hPa^{-1} to km^{-1}
    - **IRSCATT_SCATTPROPERTIES.F90**
      - Cycle through input aerosol profiles and determine single scattering properties.
      - Combine single scattering properties from different aerosols
    - **IRSCATT_INIEDD.F90**
      - Calculate B0, B1, Bn for each layer
      - Perform delta scaling of single scattering properties.
      - Calculate lambda, tau, h
      - Find uppermost scattering layer ($\omega > 0$)
    - Calculate surface flux emissivity
  - **IRSCATT_EDDINGTON.F90**
    - Calculate upwelling and downwelling radiance incident on scattering layers
    - Calculate source terms with out scattering
    - **IRSCATT_BOUNDARYCONDITIONS.F90**
      - Solve big system of linear equations
    - **IRSCATT_INTEGRATESOURCE.F90**
      - Integrate source terms.
    - Integrate radiance
  - Convert radiance to BTs

Table A2 Structure of RTTOV8_IRS program.

Type	Variable	Description
profile_aerosol_type		
Integer	naerosol	number of aerosol components
Integer	aerosol_type(:)	type of each component
Real	conc(:,:)	extinction coefficient (km^{-1} at 10 µm)

Table A3 Definition of aerosol profile structure.

Type	Variable	Description
Irscatt_opac_coeff		
Character	id_Common_name	name of aerosol/cloud component
Integer	nrelhum	number of relative humidity levels
Real	ext(:,:)	extinction coefficient (n_channels, nrelhum)
Real	ssa(:,:)	single scattering albedo
Real	asm(:,:)	assmetry parameter

Table A4 Definition of optical properties lookup table structure.

Appendix 2

Simulations of aerosol impact on BTs, **k** , in kelvin, for different base altitudes of the aerosol layer, aerosol optical depth, and zenith angle. Results are given for two sets of aerosol characteristics, OPAC and Haywood (see main text for details).

Zenith = 0 AOD = 0.1

Base altitude of aerosol layer / km	0		1		2		3	
Element of **k**	OPAC	Haywood	OPAC	Haywood	OPAC	Haywood	OPAC	Haywood
3.9 µm	-0.25	-0.24	-0.29	-0.26	-0.32	-0.29	-0.36	-0.31
8.7 µm	-0.11	-0.13	-0.25	-0.32	-0.42	-0.52	-0.60	-0.74
11 µm	-0.37	-0.28	-0.55	-0.46	-0.74	-0.66	-0.93	-0.87
12 µm	-0.24	-0.19	-0.42	-0.30	-0.64	-0.43	-0.85	-0.55

Zenith=0 AOD = 0.5

Base altitude of aerosol layer / km	0		1		2		3	
Element of **k**	OPAC	Haywood	OPAC	Haywood	OPAC	Haywood	OPAC	Haywood
3.9 µm	-1.19	-1.14	-1.39	-1.28	-1.59	-1.41	-1.78	-1.55
8.7 µm	-0.46	-0.56	-1.16	-1.42	-1.97	-2.40	-2.82	-3.43
11 µm	-1.47	-1.11	-2.34	-1.99	-3.29	-2.97	-4.23	-3.97
12 µm	-0.96	-0.84	-1.83	-1.38	-2.84	-1.98	-3.89	-2.59

Zenith=0 AOD = 1.0

Base altitude of aerosol layer / km	0		1		2		3	
Element of **k**	OPAC	Haywood	OPAC	Haywood	OPAC	Haywood	OPAC	Haywood
3.9 µm	-2.19	-2.15	-2.65	-2.47	-3.09	-2.78	-3.51	-3.07
8.7 µm	-0.80	-0.96	-2.11	-2.52	-3.62	-4.34	-5.22	-6.25
11 µm	-2.34	-1.79	-3.99	-3.41	-5.80	-5.25	-7.61	-7.14
12 µm	-1.55	-1.44	-3.14	-2.48	-5.02	-3.65	-6.97	-4.83

Zenith = 48 AOD = 0.1

Base altitude of aerosol layer / km	0		1		2		3	
Element of **k**	OPAC	Haywood	OPAC	Haywood	OPAC	Haywood	OPAC	Haywood
3.9 µm	-0.44	-0.42	-0.51	-0.47	-0.57	-0.51	-0.63	-0.55
8.7 µm	-0.15	-0.18	-0.36	-0.44	-0.61	-0.75	-0.87	-1.07
11 µm	-0.57	-0.41	-0.86	-0.69	-1.18	-1.01	-1.48	-1.33
12 µm	-0.35	-0.29	-0.63	-0.47	-0.96	-0.67	-1.30	-0.86

Zenith=48 AOD = 0.5

Base altitude of aerosol layer / km	0		1		2		3	
Element of **k**	OPAC	Haywood	OPAC	Haywood	OPAC	Haywood	OPAC	Haywood
3.9 µm	-1.96	-1.89	-2.32	-2.15	-2.65	-2.40	-2.94	-2.60
8.7 µm	-0.62	-0.74	-1.60	-1.91	-2.75	-3.30	-3.96	-4.76
11 µm	-2.19	-1.59	-3.51	-2.86	-4.97	-4.31	-6.36	-5.76
12 µm	-1.33	-1.20	-2.58	-2.04	-4.08	-3.01	-5.60	-3.93

Zenith=48 AOD = 1.0

Base altitude of aerosol layer / km	0		1		2		3	
Element of **k**	OPAC	Haywood	OPAC	Haywood	OPAC	Haywood	OPAC	Haywood
3.9 µm	-3.42	-3.38	-4.14	-3.92	-4.84	-4.44	-5.44	-4.86
8.7 µm	-1.07	-1.25	-2.79	-3.25	-4.86	-5.68	-7.04	-8.24
11 µm	-3.35	-2.47	-5.64	-4.64	-8.24	-7.22	-10.73	-9.79
12 µm	-2.08	-2.02	-4.18	-3.54	-6.81	-5.33	-9.46	-7.04

Zenith = 60 AOD = 0.1

Base altitude of aerosol layer / km	0		1		2		3	
Element of **k**	OPAC	Haywood	OPAC	Haywood	OPAC	Haywood	OPAC	Haywood
3.9 µm	-0.55	-0.53	-0.66	-0.61	-0.76	-0.68	-0.83	-0.74
8.7 µm	-0.12	-0.14	-0.40	-0.48	-0.73	-0.89	-1.08	-1.31
11 µm	-0.65	-0.44	-1.06	-0.82	-1.51	-1.26	-1.92	-1.68
12 µm	-0.34	-0.30	-0.71	-0.55	-1.17	-0.84	-1.63	-1.10

Zenith=60 AOD = 0.5

Base altitude of aerosol layer / km	0		1		2		3	
Element of **k**	OPAC	Haywood	OPAC	Haywood	OPAC	Haywood	OPAC	Haywood
3.9 µm	-2.39	-2.32	-2.90	-2.71	-3.39	-3.09	-3.76	-3.36
8.7 µm	-0.52	-0.62	-1.73	-2.05	-3.19	-3.79	-4.74	-5.63
11 µm	-2.43	-1.67	-4.13	-3.26	-6.09	-5.15	-7.88	-7.01
12 µm	-1.29	-1.25	-2.83	-2.34	-4.79	-3.67	-6.73	-4.89

Zenith=60 AOD = 1.0

Base altitude of aerosol layer / km	0		1		2		3	
Element of **k**	OPAC	Haywood	OPAC	Haywood	OPAC	Haywood	OPAC	Haywood
3.9 µm	-4.01	-4.00	-4.97	-4.76	-5.93	-5.49	-6.68	-6.03
8.7 µm	-0.95	-1.11	-2.96	-3.40	-5.48	-6.31	-8.13	-9.35
11 µm	-3.62	-2.55	-6.37	-5.12	-9.64	-8.29	-12.67	-11.40
12 µm	-2.00	-2.08	-4.44	-3.96	-7.68	-6.31	-10.87	-8.50